Thermal structure of the Aegean lithosphere from numerical modelling

06-07-2018

Victor Larède
3818705

Earth, Structure & Dynamics

Abstract

The Aegean offshore area has a relatively thin crust and shallow Moho. This shows opportunities for geothermal energy exploration and exploitation, but first requires a better understanding of the thermal structure of the lithosphere. A geological model of the crust in the Aegean offshore region is constructed, from existing literature. This serves as an input geometry to model the steady-state temperature distribution of the lithosphere in the area. Information on their composition of the crust and its thermal properties is gained from literature. A horizontal resolution of 5000 by 5000 m and a vertical cell spacing of 400 m are set to model the region. A surface temperature of 10 C and a thermal Lithosphere-Astenosphere boundary (LAB) temperature of 1330 °C are used as boundary conditions. Multi 1-D numerical modeling is performed to pre-process the input-data, to finally construct four 3-D temperature models, with a varying depth of the LAB. The models have implications to whether conduction would be the dominant heat transfer mechanism given the prescribed circumstances. They show possible intermediate to cold regions in the north, hot to intermediate regions in the central Aegean, a generally cold region from the central Aegean towards the south, except in the outermost south where a possible hot region is present.

Contents

1 Introduction

Using gravimetric inversion, Tirel et al. (2004) has mapped the crustal thickness and Moho topography (Figure 1) of the Aegean region showing, except for some small localized deviations, a relatively homogeneous thin crust throughout this region.This suggests the presence of a high thermal gradient. What was already proposed byJongsma (1974), who measured a high heat flow on several locations in the Aegean Offshore area, especially within and behind the Cycladic volcanic arc. Overall, his research pointed out that heat flow increases from the Hellenic trench towards the North. This might provide opportunities for geothermal energy exploration and exploitation of the Aegean, which, however, first requires a better understanding of its thermal structure. A model structural model is constructed of the crust in the offshore Aegean region, containing the main units in the area and as much information available on their composition and thermal properties, in order to make a steady-state 3-D thermal model of the lithosphere in the area.

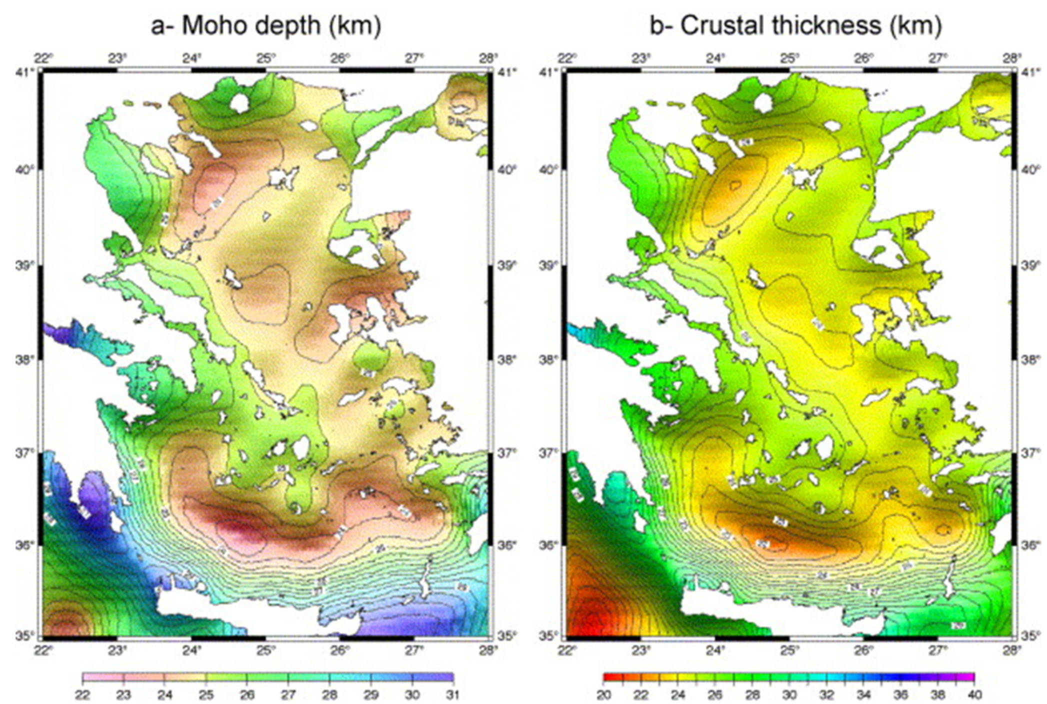

Figure 1: Moho depth (a) and crustal thickness (b), from (Tirel et al., 2004)

1.1 Tectonic setting

The Aegean (sea) region (Figure 1) is considered as one of the back arc basins of the Mediterranean subduction system (Jolivet and Brun, 2010). The region is generally subdivided into 3 continental blocks (Rhodope, Pelagonia and Adria) with 2 oceanic sutures in between them (the Vardar suture zone (VSZ) and the Pindos suture zone (PSZ)) (Philippon et al., 2012, 2014; Brun et al., 2016). Anatolia enters the Aegean through westward movement via the North Anatolian fault(NAF) (Beniest et al., 2016), which propagated into the area around 5-6 Ma ago (Jolivet et al., 2013), but already contributes to the structure of the area since mid Miocene (Beniest et al., 2016). Currently, Anatolia is extruding westward at 2.1 cm*yr^{-1} with respect to Eurasia (Philippon et al., 2014; McClusky et al., 2000). The study area is thought to have been formed, not solely but largely, as a consequence of the subduction and southward retreat of a large slab (consisting of several domains) (Faccenna et al., 2003; van Hinsbergen et al., 2005; Jolivet and Brun, 2010). Tomographic models show a single slab of more than 1500 km long, suggesting one single subduction active during the Cenozoic in which several domains have either been subducted or accreted to the southern margin of Eurasia (Jolivet and Faccenna, 2000; van Hinsbergen et al., 2005; Jolivet and Brun, 2010). The subduction is caused by the convergence between the Eurasian an African plates (van Hinsbergen et al., 2005). Also, the area has experienced several stages of (backarc) extension, due to southward retreat (McKenzie, 1978; Le Pichon and Angelier, 1979; Le Pichon et al., 1981) of the Hellenic trench caused by slab roll-back of the African plate, since the last 45 Ma. Southward movement of the Hellenic trench is nowadays at a pace of circa 3.3 cm*yr^{-1} (Philippon et al., 2014; McClusky et al., 2000) and has already traveled a distance of roughly 700 km, which can be seen from the shift of volcanism towards the South (Fytikas et al., 1984; Brun and Sokoutis, 2010). Combined with westward movement of Anatolia, this process has stretched and rotated the region to its current position (Brun and Sokoutis, 2010; Philippon et al., 2014). It has caused thinning of the lithosphere, the formation of extensional basins, exhumation of metamorphic core-complexes, for example in the Cyclades, Rhodope and Menderes (Brun and Sokoutis, 2010; Brun and Faccenna, 2008; Tirel et al., 2004). The Cycladic Blueschist Unit (CBU) is currently located in the central Aegean, south of the North Cycladic Detachment (NCD), on the boundary between Pelagonia in the north and Adria in the south (Jolivet and Brun, 2010; Philippon et al., 2012). There, a metamorphic ophiolitic mélange of the Pindos ocean is present which was exposed to blueschist- and eclogite facies metamorphism(Philippon et al., 2012; Bonneau and Kienast, 1982).
A large part that is now located in the overriding plate and making up the present Aegean area, has been part of the plate that is being subducted, and was scraped of or exhumed during the process (van Hinsbergen et al., 2005; Jolivet and Brun, 2010; Jolivet et al., 2013). It has been subducting underneath Crete and the Mediterranean ridge from around Oligocene times(Le Pichon et al., 1981; Gautier et al., 1999; Jolivet and Faccenna, 2000; Jolivet and Brun, 2010)

Currently, the crust is relatively thin throughout the whole offshore area. Maxima are at the Cyclades (Tirel et al., 2004), and the sides where it gets thicker towards the mainland and Crete, and minima are at the North Aegean Through and the Cretan sea where it gets very thin (Jolivet and Brun, 2010; Tirel et al., 2004).

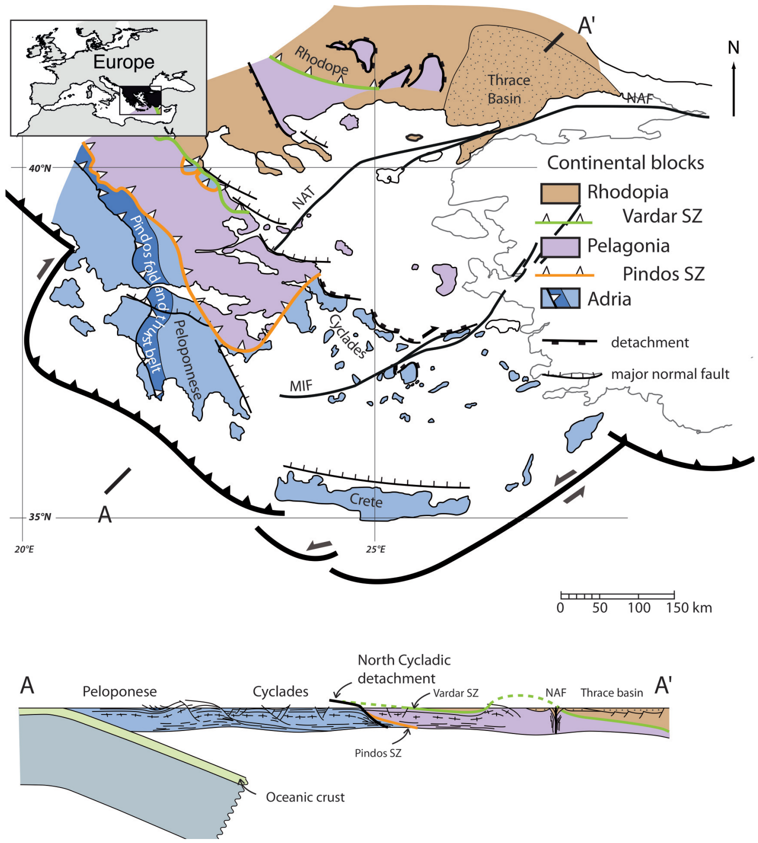

Figure 2: Map and cross-section of the Aegean area from (Brun et al., 2016)

1.2 Tectonic evolution

Around 65 Ma ago subduction was taking place in the very north of the area, and after the closure of the Tethys and Vardar ocean, which were being subducted below Eurasia (van Hinsbergen et al., 2005), and eventually led to the formation of the VSZ (Philippon et al., 2012). The Pelagonian domain entered the subduction zone and remnants of the Tethys and Vardar were thrusted on top of it(van Hinsbergen et al., 2005; Jolivet and Brun, 2010; Menant et al., 2016) Further north, ultra high-pressure rocks that were already exhumed near Rhodope (Brun and Sokoutis, 2007) became part of the upper crust (Jolivet and Brun, 2010). The VSZ can nowadays probably be followed as far as the Turkish mainland, where it turns into the Izmir Suture zone (ISZ) (Philippon et al., 2014; Menant et al., 2016), see fig. 4. At roughly the same timing, the relative movement between Eurasia and Africa almost ceased, pausing the compressional regime. This is probably the moment that the slab started to roll back, driven by its own weight (keeping subduction going) (Jolivet and Brun, 2010). More to the south of Pelagonia, the Pindos and Gavrovo-Tripolitza platform, which likely contained a phyllite-quartzitic basement platform, were located. Around 50 Ma ago, as convergence returned, the Pindos ocean started to subduct fast. At this stage the Pindos oceanic crust is reworked to become blueschists and eclogites at depth. Coinciding with the return of convergence, and even though the Balkan region experienced compression, Rhodope experienced extension, making way for core complexes to start forming (Jolivet and Brun, 2010). The slab started to retreat southward quickly, at around 35 Ma, as the absolute movement of the African plate slows down. Thrusting was going on towards the south affecting the Gavrovo-Tripolitza Platform, understacking Phyllite-Quartzite units which will later be exhumed underneath Crete (Jolivet and Brun, 2010). Consequently, as the trench moved southward, magmatism also moved southward (Brun and Sokoutis, 2010; Jolivet and Brun, 2010). Weakening of the crust due to partial melting allowed the Moho to remain flat and core complexes to develop (Brun and Sokoutis, 2007) in the Cyclades (Jolivet and Brun, 2010). Granodiorite started to intrude the cycladic core complexes, around 23 Ma. Rhodope experienced a more brittle extension and sedimentary basins form at the core complexes. In Crete, exhumation was still going on, but also sediments are deposited (Jolivet and Brun, 2010). As slab retreat continued, extension is more focused on the Cretan sea area from around 10 Ma (Jolivet and Brun, 2010). (Syn-orogenic) Exhumation took place during subduction in the subduction zone via subduction channel tectonics in the Cyclades, Peloponnese and Crete during the Eocene, Oligocene and Early Miocene respectively, whereas the last (Post-orogenic) exhumation was in the back-arc (Jolivet and Brun, 2010).

1.3 Structuration of the Aegean crust

As mentioned in section 1.1, in a first order approach the Aegean crust can be described by only 2 or 3 continental units and 2 oceanic sutures; Rhodope, Pelagonia, Adria, the Vardar Suture zone and the Pindos Suture zone e.g. (Philippon et al., 2012; Brun et al., 2016), see fig. 4. The most important basins in the north are the Thermaikos basin, the Northern Aegean Trough basin (fig. 7), which is bounded by The North Anatolian Fault, and the Northern Skyros basin. The Ikaria basin in located in the more central part of the Aegean sea and lastly the Cretan basin is located in the south, near Crete in the Cretan sea.

Rhodope lies in the northern part of the area, is located at the boundary of the area of interest and extends further north onshore. The extend of Rhodope in the offshore area is not very well defined, but through the available cross-sections and maps of the area (Fig. 2, 3a and 3b) from Brun et al. (2016) and Menant et al. (2016), an attempt has been made to extrapolate it to offshore region. Towards the south, the Vardar suture zone separates Rhodope from Pelagonia (Fig. 4), which extents up to the North Cycladic Detachment (NCD). There the Cyclades and the Cycladic Blueschist Unit (CBU) are present on the Ardiatic side, the CBU probably represents the passive margin of the Pindos Ocean.

Adria is the most southern continental block and contains 3 units at the surface; CBU and the Cyladic basement which is combined with the Gavrovo-Tripolitza Unit, this will be discussed in section 2.2.

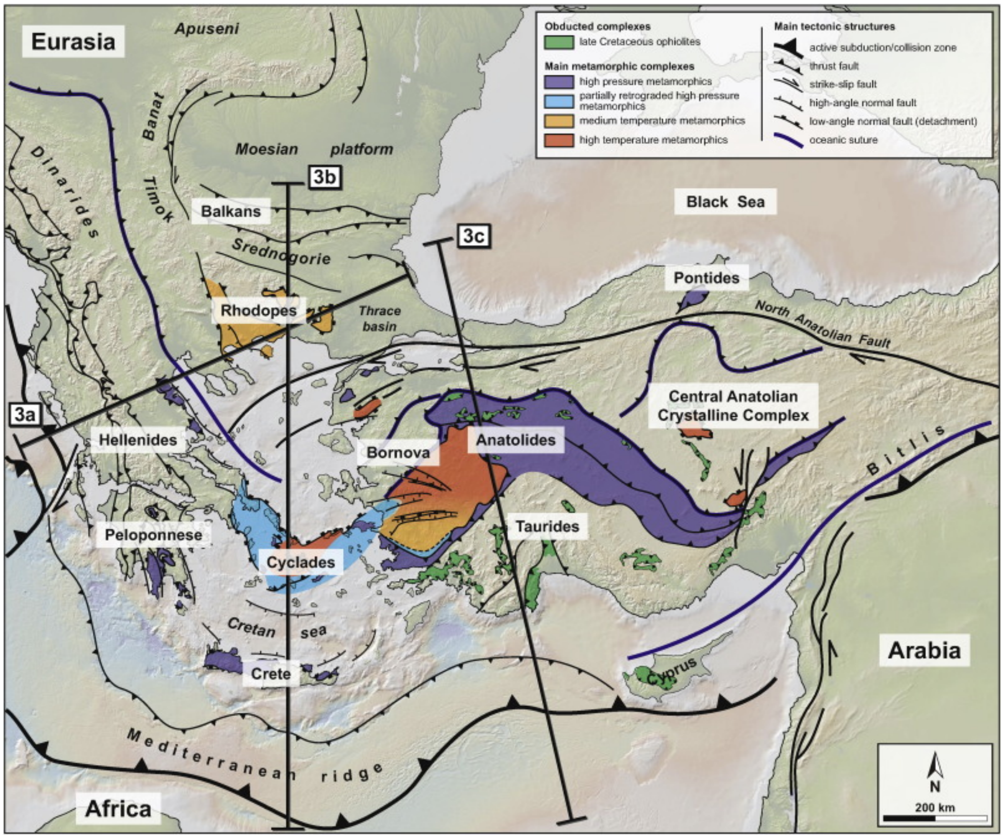

(a) The research area from (Menant et al., 2016) concerning the Aegean region and surroundings. the Lines are corresponding to the cross-sections in fig. 3b

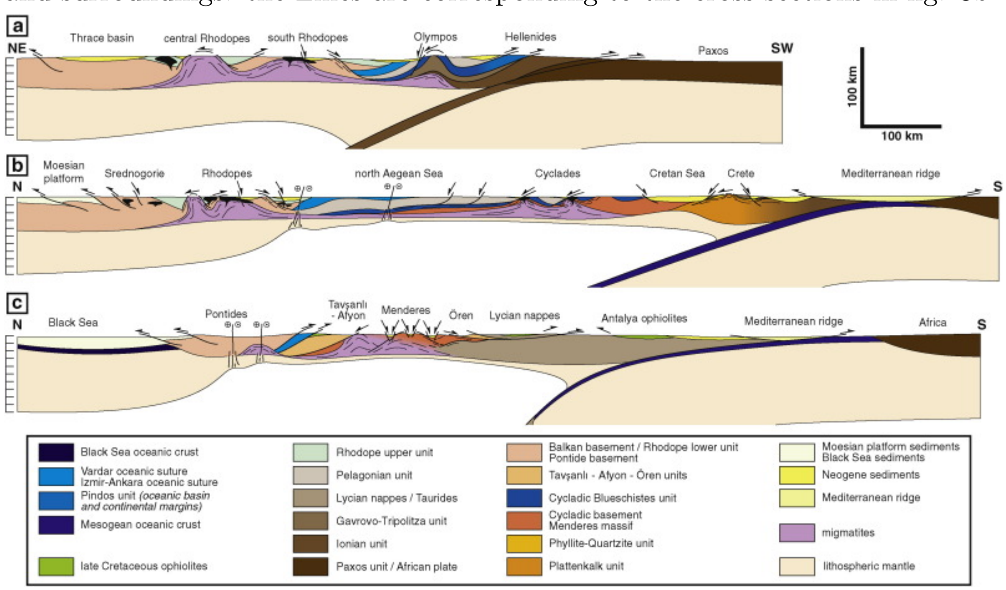

(b) Vertical cross-sections from (Menant et al., 2016) drawn in fig. 3a

Figure 3: Tectonic map with cross-sections of the eastern Mediterranean region with cross-sections, from (Menant et al., 2016)

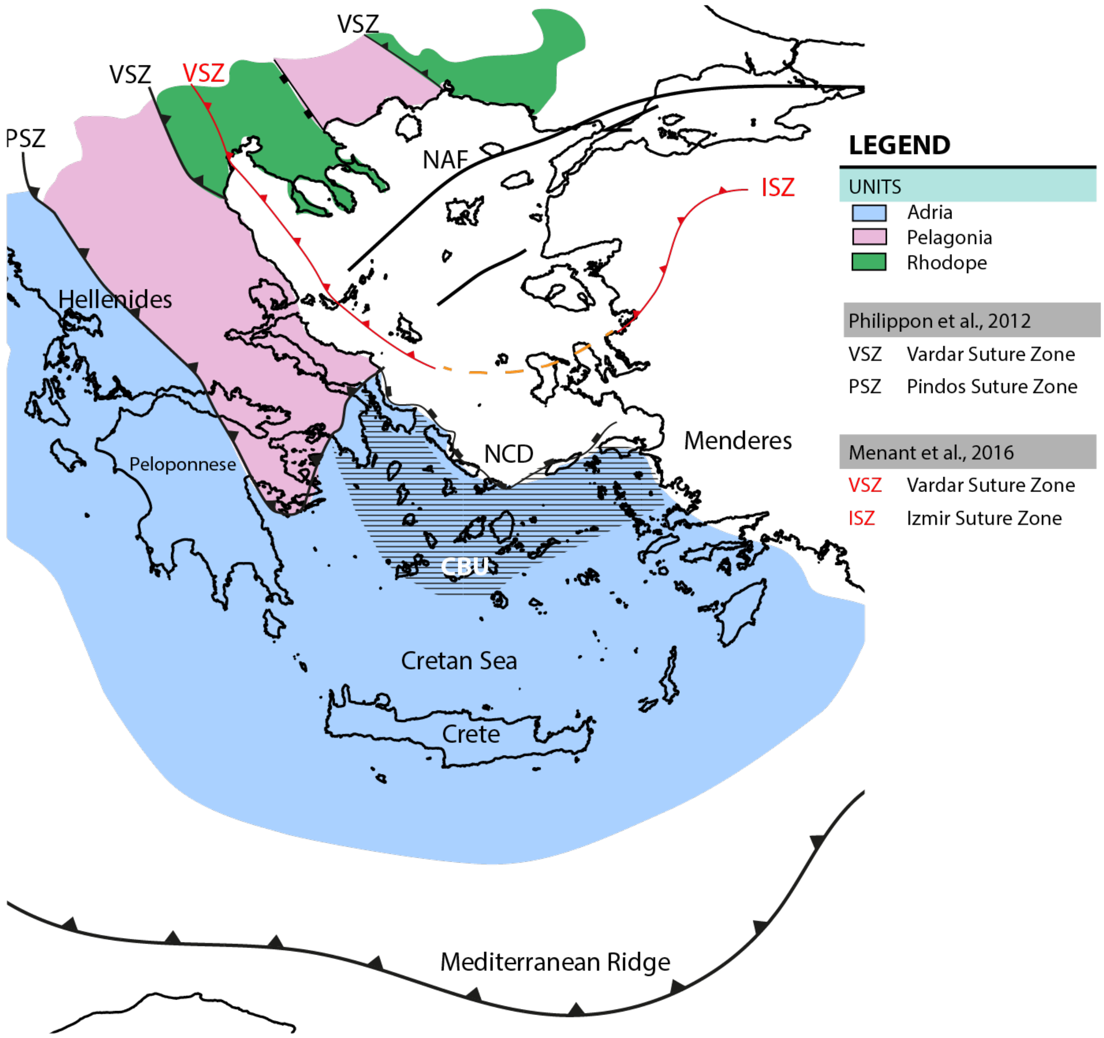

Figure 4: The Aegean region with its main tectonic features, based on maps from (Philippon et al., 2012) and (Menant et al., 2016), the shaded area is the region of the Cycladic Blueschist Unit (CBU).

2 Geological model of the Aegean region

To model the temperature distribution in the Aegean region, a geological model of the lithosphere is needed, containing the main lithologies to define the transport and production of heat in the defined layers. Since no raw data available for the purpose of this research, the whole model is based on data obtained from literature e.g. Tirel et al. (2004); van Hinsbergen et al. (2005); Brun and Sokoutis (2010); Jolivet and Brun (2010); Jolivet et al. (2013); Beniest et al. (2016); Menant et al. (2016). The crustal units in the model are largely based on the information on the nonmetamorphosed (van Hinsbergen et al., 2005) Hellenides, which are on the mainland of Greece, West/Southwest of the Aegean sea (Figure 2, 3, 4 and 5). Since the information on the proportions of the crustal units & basins and their compositions isn't specified in great detail, the input-model will be a first order approximation. The topography thats is used comes from ETOPO1 (Amante and Eakins, 2009) and the depth of the Moho was taken from the work of Tirel et al. (2004).

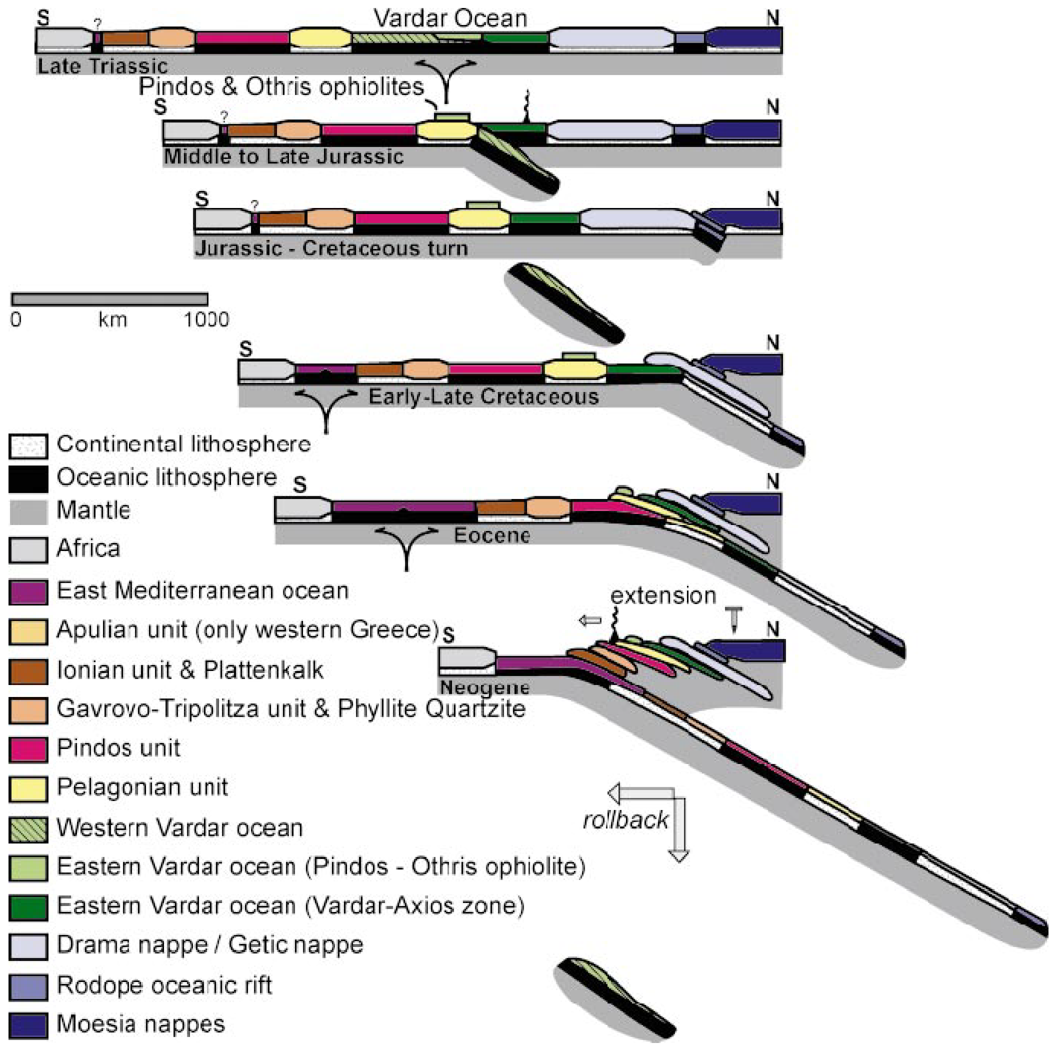

Figure 5: Evolution of the Aegean nappe stack, from (van Hinsbergen et al., 2005)

2.1 Workflow

Georeferencing

To extract information from maps as the ones from Beniest et al. (2016); Brun et al. (2016); Menant et al. (2016), e.g. see fig. 6, they had to be georeferenced in order to relate them to geographical coordinates. This was done using the software ArcMap 10.1. The coordinate reference system used in this research was *WGS84/UTM Zone 34N*. This is a Cartesian coordinate system, and this is needed for the thermal modeling software (B3t). With the georeferenced maps, geological model of the region could be constructed using GeoModeller.

GeoModeller 4.0.1

GeoModeller is a software to build, among other things, 3-D geological computer models. Depending on the licences one works with, there are more features that can be used, such as geophysical modelling. But for the purpose of this research, it was only used to built a 3-D model of the crust.

First, the coordinate system was put in; *WGS84/UTM Zone 34N*. Then, a volume with an extent of (612700.0, 3901800.0; 1102700.0, 4549800.0), a height of 4000 [m] and a depth of 100000 [m] w.r.t. sea-level was defined, in which the geological model could be constructed. The surface topography layer from Amante and Eakins (2009) was used to bound the top of the geological model. A stratigraphic pile of the crustal units and sedimentary basins was prescribed, these are discussed in section 2.2. Georeferenced (surface) maps were inserted to take over their geological data. Horizontal lines were drawn representing vertical sections. On those vertical sections, images of cross-sections were projected to take over their geological data as well. Finally, the software computed and built the 3-D model by interpolating the inserted information that was given on the various sections using a potential field method. The layers constructing the model were exported as .asc-files

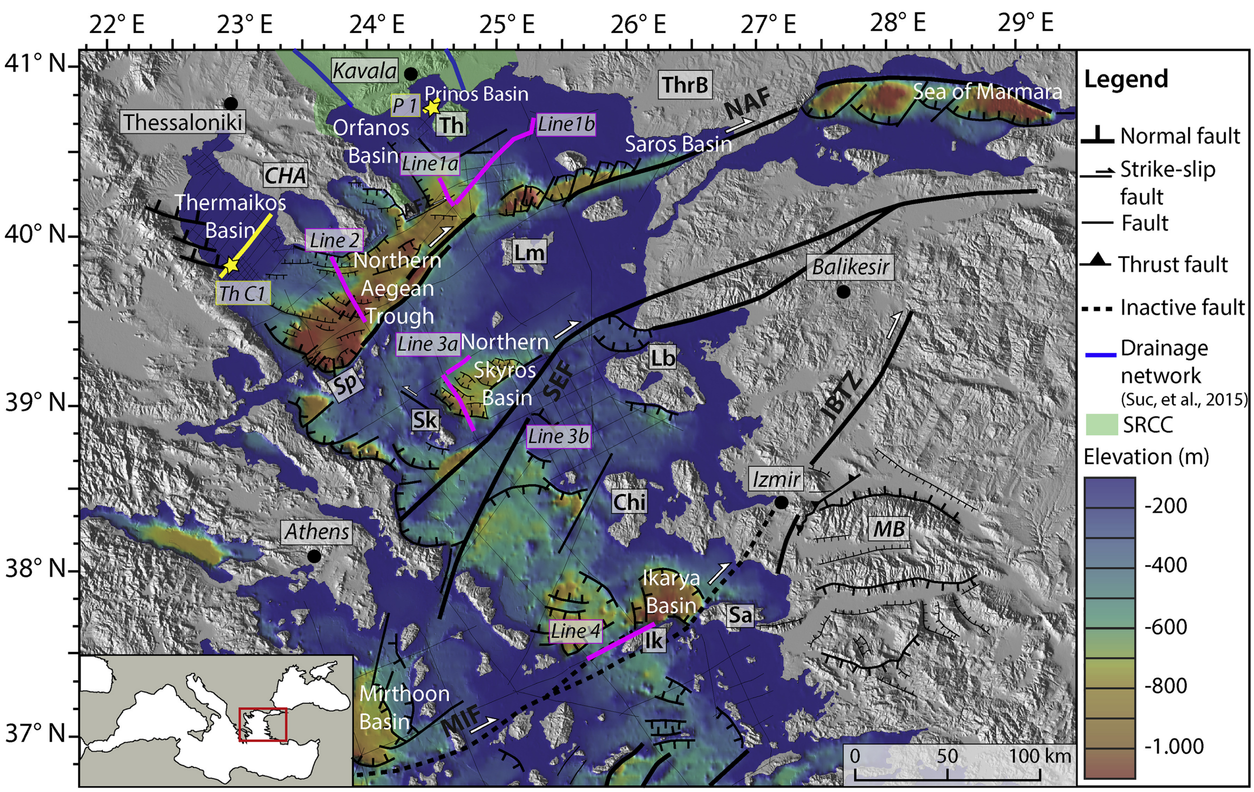

Figure 6: Digital elevation model of the study area of Beniest et al. (2016), with the main fault systems.

3-D structure

In GeoModeller, the topography of Amante and Eakins (2009) was used to constrain the top of the crust. Several vertical cross-sections from the literature, as well as own interpretations, were used to constrain the crustal units.

One of the shortcomings of using GeoModeller in terms of constructing the crustal units, was the usage of a stratigraphic pile. This is used for the extrapolation of the different units present in the area. However, this pile puts a constraint on the succession of the units. In this research the succession of the different units wasn't always the same (continuous) in every place. This was sometimes problematic, when computing the model, because units would be extrapolated to places where they shouldn't exist. This will also be adressed in the discussion with a figure (fig. 22). To avoid these difficulties one should keep the geometries and transitions of the units drawn on the sections as simple and smooth as possible.

2.2 Structure and composition of the Aegean lithosphere

The geometry of the crustal model is defined by 4 layers. A sedimentary layer at the top, consisting of 5 sedimentary basins. An upper crustal layer, consisting of 5 units. A lower crustal layer, consisting of 1 unit. And a layer of 1 unit defining the lithospheric mantle. Figure 7 and 12 present the surface maps containing the basins and crust units in the area. And figure 13 shows vertical cross-sections through the area, which are drawn in fig. 12 The choices regarding the lithologies assigned to each layer are explained in the sections below, and listed in tables 2 and 1

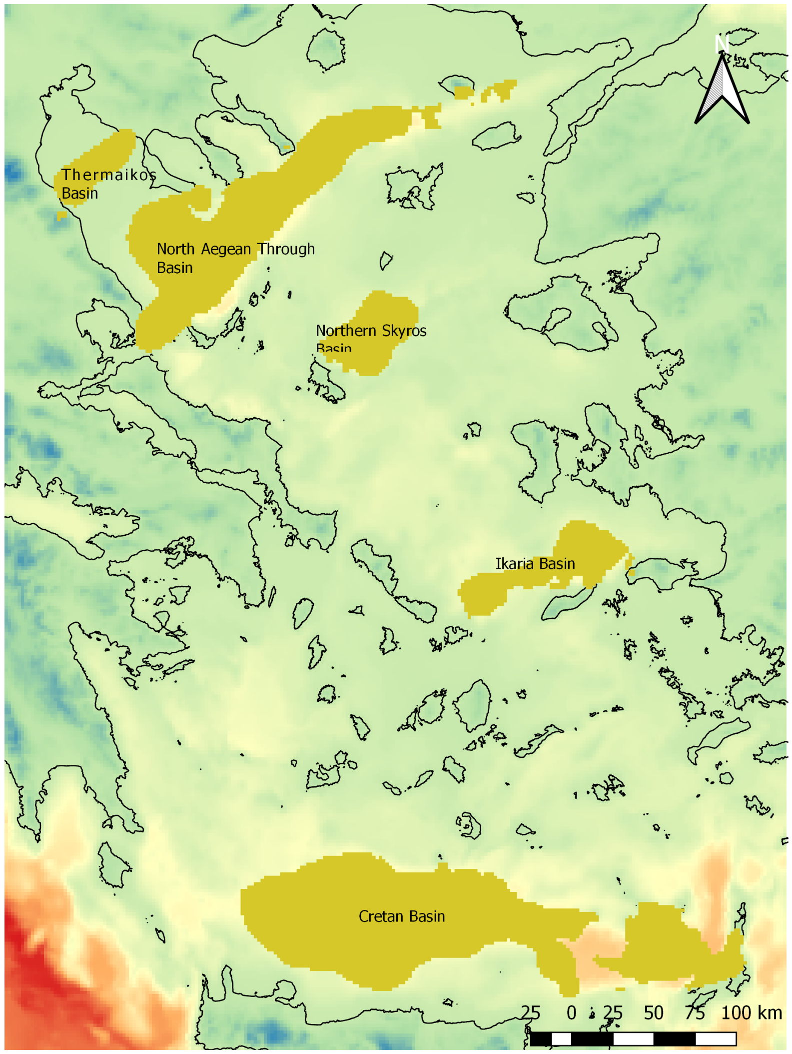

Figure 7: Map of the main basins in the Aegean sea area that are considered in this research, basin on Hsü et al. (1978), Makris et al. (2013) & Beniest et al. (2016).

2.2.1 Sedimentary basins

Some information on basins/sediments is considered in the input-model. The following basins have been included, see fig. 7; the Thermaikos basin and Northern Aegean Trough basin in the north, the Ikaria Basin and the Northern Skyros Basin in the central Aegean, and the

Cretan basin in the south. The ages of the sediments in the different basins are varying. The oldest sediments considered were deposited from the Eocene and onwards and all of them are assigned an acoustic basement, which is associated with metamorphic Mesozoic rocks onshore but no stratigraphic information can be given of shore because no well data was available at this depth (Beniest et al., 2016).

The information on each basin has been retrieved from interpretations by Beniest et al. (2016)[and the references therein], and Hsü et al. (1978) specifically for the Cretan sediments. These papers are based on existing literature, seismic reflection datasets, well logs and drillings. The thicknesses of the sediments in the input model have been based on the work by (Hsü et al., 1978; Makris et al., 2013; Beniest et al., 2016)

Although the stratigraphic columns of, for example Beniest et al. (2016), contain valuable information for the input model, the uncertainty about the composition of the sediments remains high. For instance, the stratigraphic columns show only distinctions between strata/sequences, but do not constrain the lithologies in detail, e.g.: fluvial, floodplain, coal, lacustrine proximal or distal, coal, carbonate platform, shallow marine, deep marine, offshore, turbidite, volcanic or evaporitic sediments (Figure 8). However, considering the dimensions of the thermal model, this doesnt have to make a huge difference. More information about certain basins is given in the paper itself, but a lot of room for interpretation is left. For the scope of this research, a first order interpretation has been done, based on the work mentioned above.

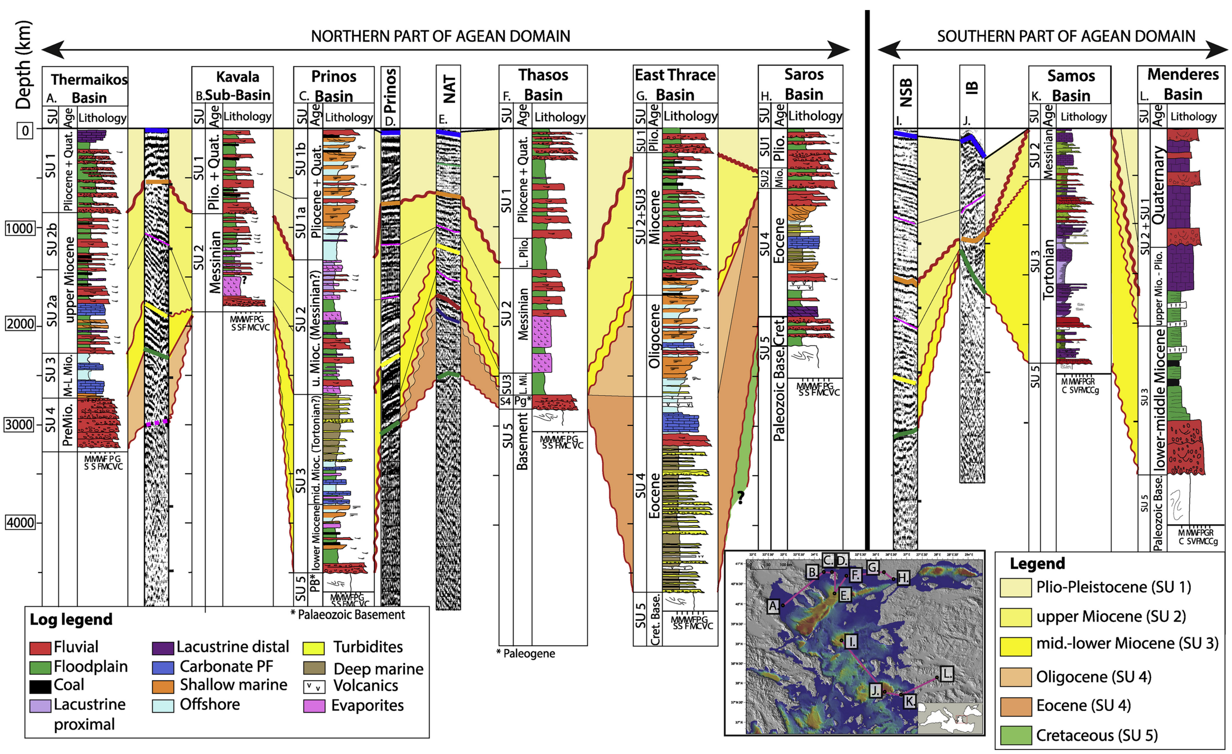

Figure 8: Well correlation done by Beniest et al. (2016), based on literature on offshore well log data and on literature on the onshore basin in the northern Aegean domain.

Thermaikos

Beniest et al. (2016) describe the upper unit as the top of a prograding system (Figure 8 and 9). Floodplain sediments are interpreted as clay rich sandstone and fluvial sediments as typical conglomerates. Although they arent abundant, coal sediments have been set to coal (pure). The carbonate platform and offshore sediments have been put in as organic rich limestones. Because the minor shallow marine are described as siliciclastic and are, as well as the lacustrine sediments, within the grain size range of the floodplain sediments, they have been assigned the same lithology as the floodplain sediments.

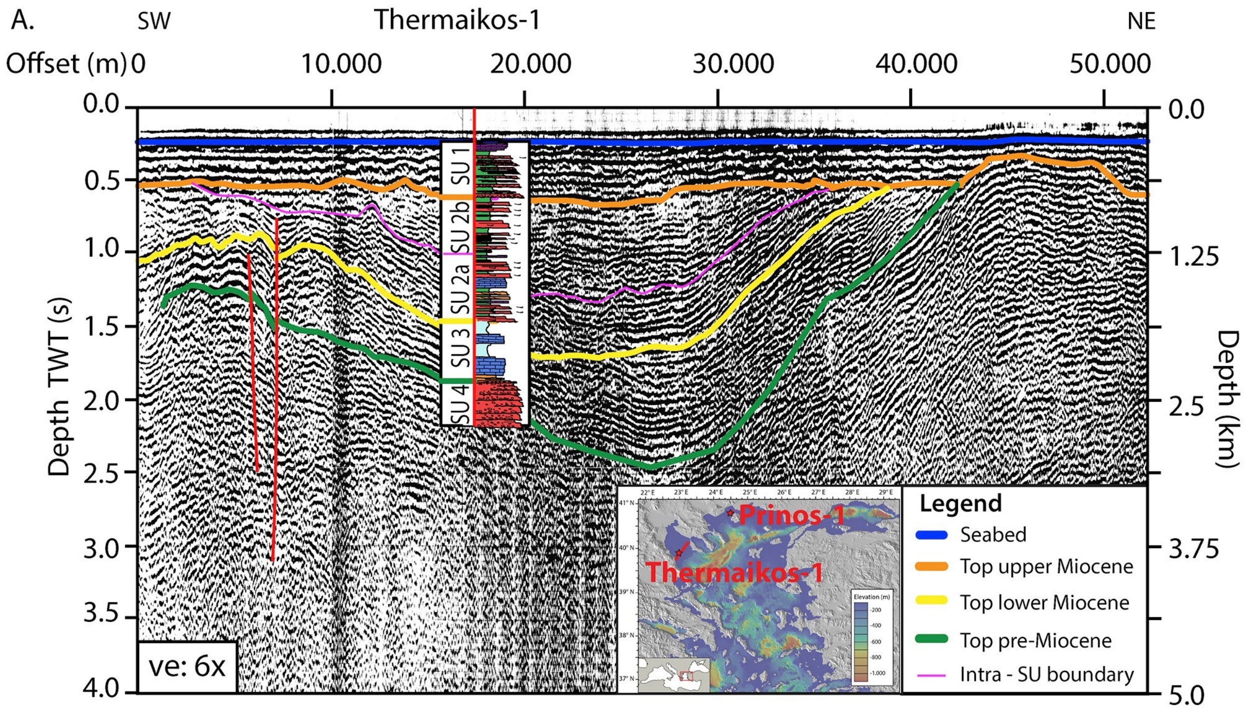

Figure 9: Interpreted seismic line of the Thermaikos basin, from Beniest et al. (2016)

Northern Aegean Trough basin

For the sake of simplicity, the stratigraphic well log of the Thasos basin (Figure 8) from Beniest et al. (2016) was mainly used to constrain the sediments of the North Aegean Trough (figure 10). Floodplain sediments have been treated as clay rich sandstones, fluvial sediments as typical conglomerates and the evaporitic layers as salt.

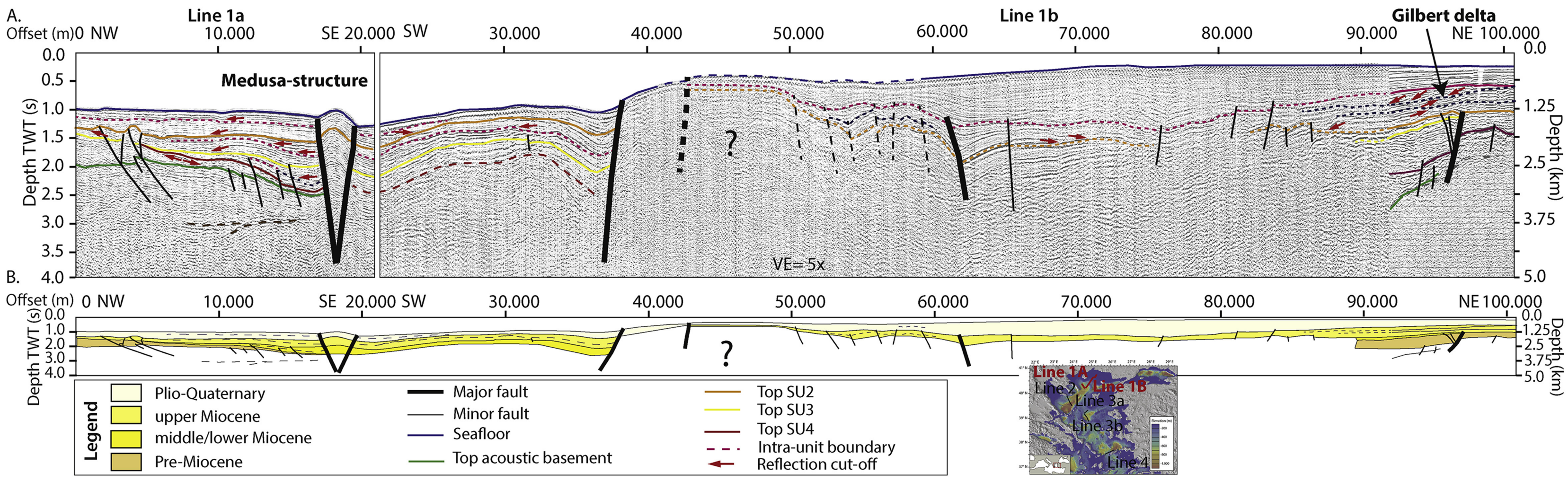

(a) line 1

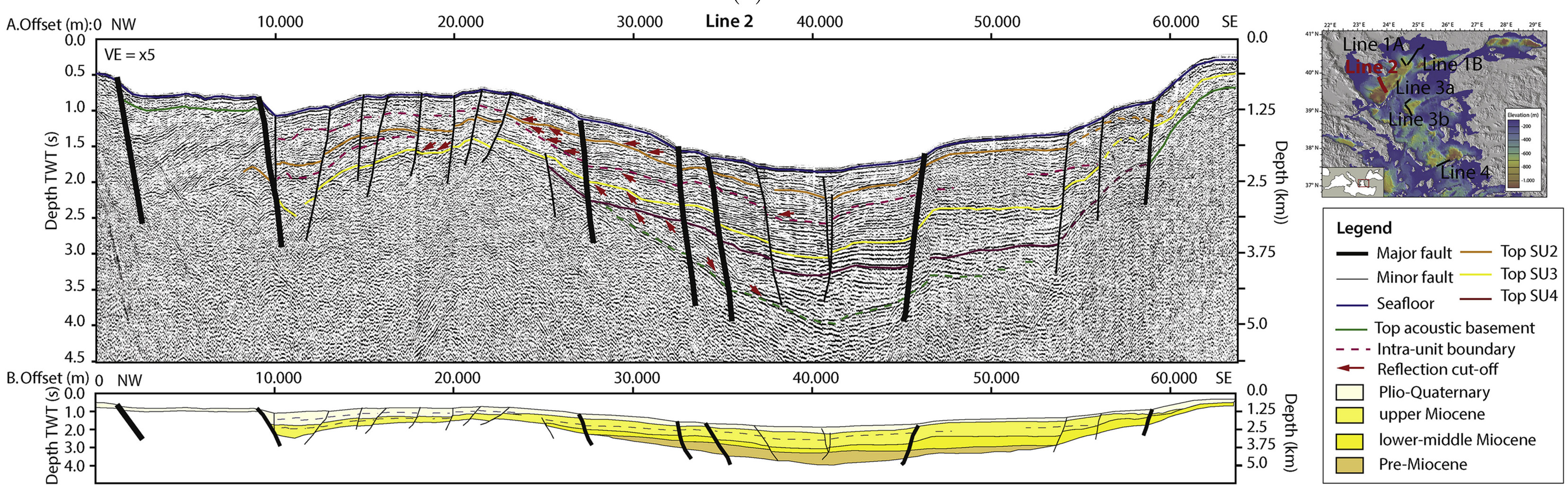

(b) Line 2

Figure 10: North Aegean Through basin seismic lines with interpretations from Beniest et al. (2016)

Northern Skyros Basin

For this basin (Figure 11a), the lithologies are correlated the Northern Aegean Trough basin sediments (Figure 8), because this basin is the closest and shows the most similarities in terms of structure e.g. normal faults, strike-slip fault. Floodplain sediments have been treated as clay rich sandstones, fluvial sediments as typical conglomerates and the evaporitic layers as salt.

Ikaria Basin

Beniest et al. (2016) cannot correlate the top part of this basin (Figure 11b) to a basin located nearby, therefore the choice is made to view the top of the basin as an alternation of fluvial and floodplain sediments, because most of the stratigraphic logs (Figure 8) show such a sequence at the top. Everything underneath is correlated with the Samos basin and consists of fluvial, floodplain and lacustrine sediments. The fluvial sediments are treated as typical conglomerates and the floodplain together with the lacustrine sediments are treated as clay rich sandstones

Cretan basin

The Cretan sediments are treated as roughly 90 percent marlstones and 10 percent gypsum, based on the interpretation of core-samples by Hsü et al. (1978). Furthermore, the basement of the basin wasn't reached in the survey described by Hsü et al. (1978). Therefore, the basin used in the model is a very rough approximation, not knowing whether it is accurate or not. However, for the purpose of this research, it is more interesting to include this basin rather than leaving it out.

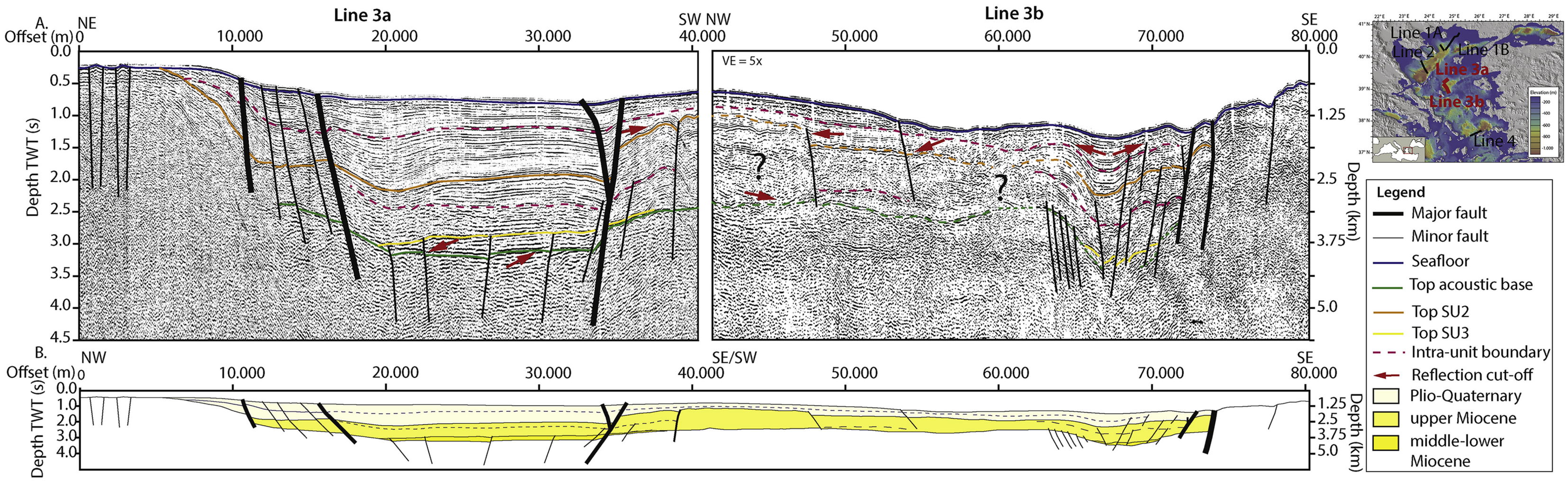

(a) Northern Skyros Basin

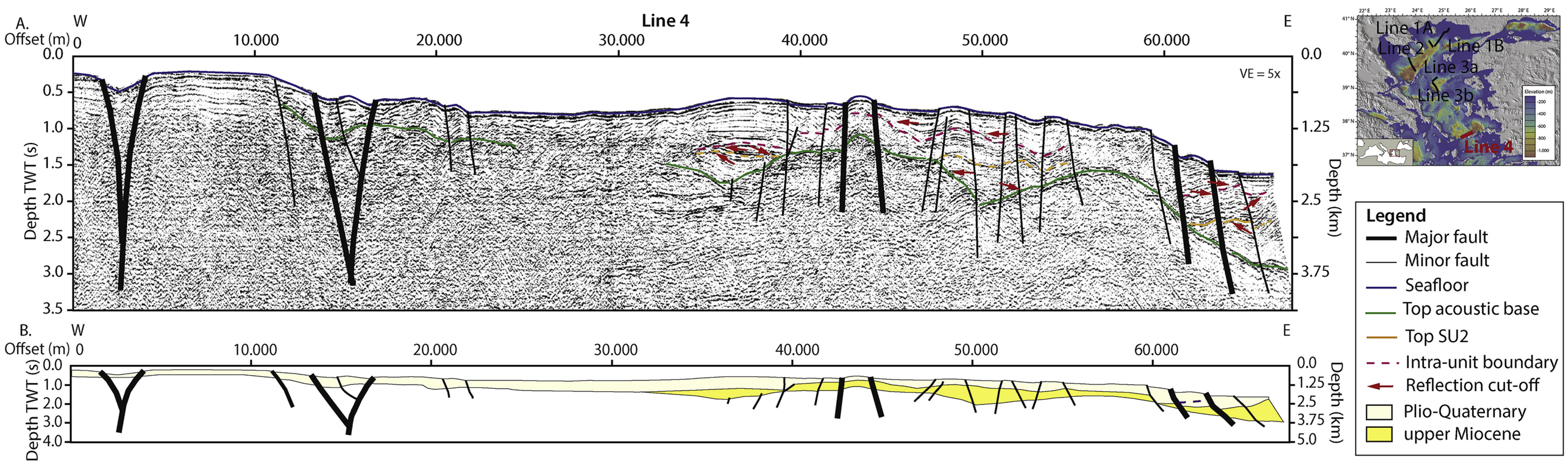

(b) Ikaria Basin

Figure 11: Northern Skyros basin and Ikaria basin seismic lines with interpretations from Beniest et al. (2016)

2.2.2 Crust

Since Oligocene times, two phases of extension have affected the Aegean area, thinning the crust (Tirel et al., 2004). The crustal model inferred by Tirel et al. (2004) shows a rather flat Moho throughout the whole area at a depth of 25 km in the Cyclades, 22 km and 24-26 km in the North Aegean. The crustal units of the input model, visualized in fig. 12 and 13, are described from north to south below. The final input is listed in table 2 in section 3.

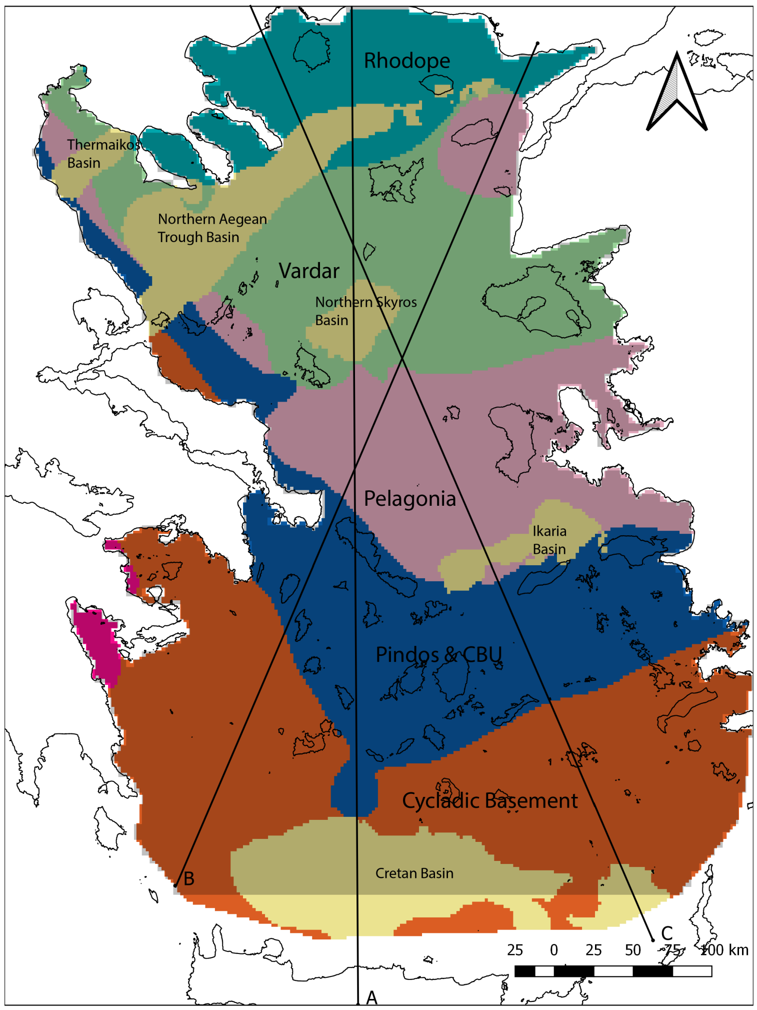

Figure 12: Map of the main crustal units and basins (see fig. 7, at the surface, only the shaded area is later used for the thermal modeling. Lines A, B, and C are the cross-sections that are shown in fig. 13

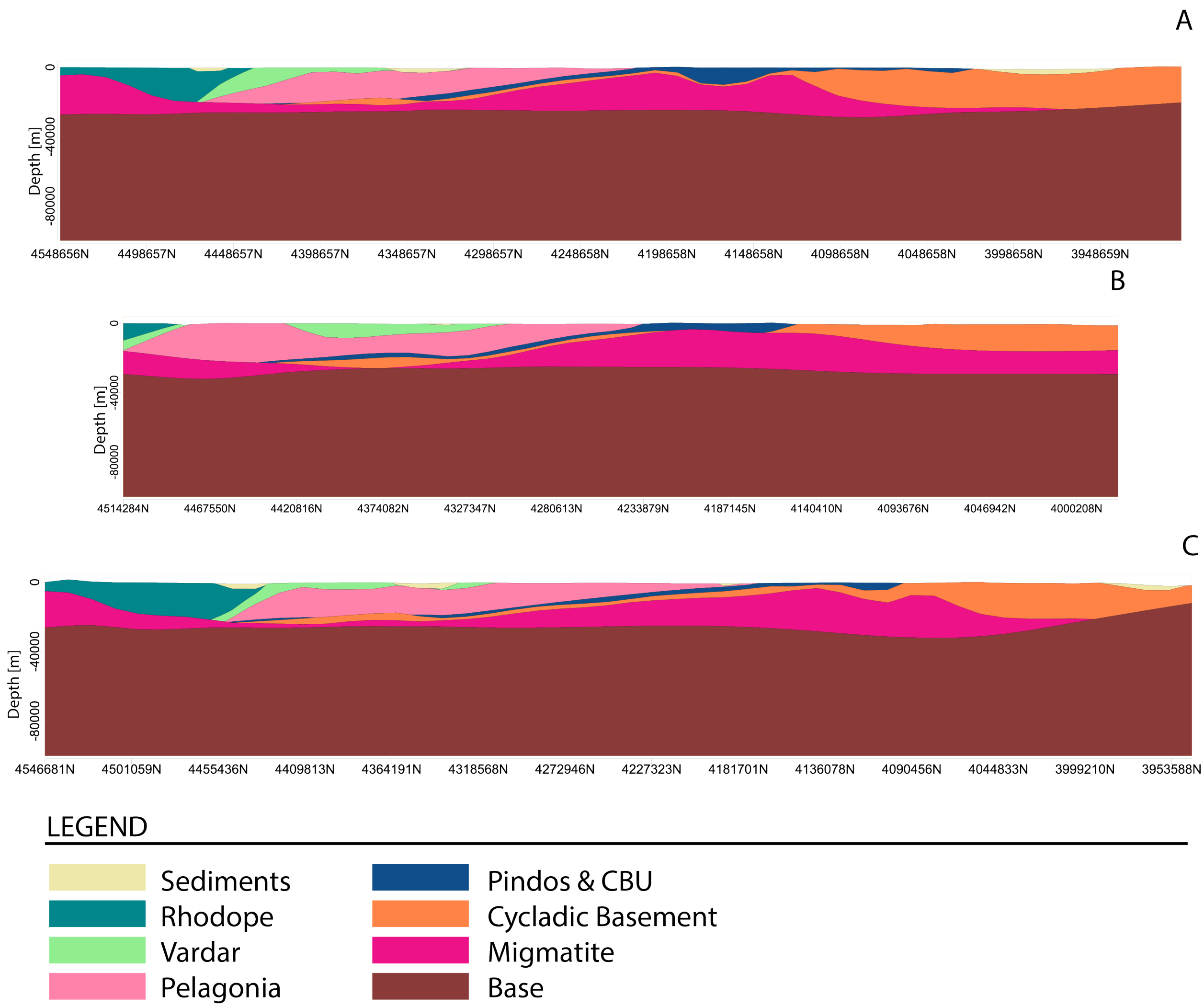

Figure 13: Vertical cross-sections corresponding to lines A, B and C in fig. 12. Note that the brown basal layer is not a fixed lithology, but defines the space in which a lithospheric mantle with varying thickness can be modeled. The other colours correspond to the colours used in fig. 12.

Rhodope

Underneath Rhodope, there is migmatite doming up, which can be clearly seen in the cross-sections of Menant et al. (2016). Brun and Sokoutis (2007) state that the Southern Rhodope core complex largely consist of units of marbles and orthogneisses and a smaller portion of schists, paragneisses and even amphibolites. In the input-model this unit is assigned a mixture of the above mentioned lithotypes of which the largest part is assigned gneiss and marble. The collection of thermal properties of rocks compiled doesn't make a distinction between the protolith of metamorphic rocks, so both orthogneiss and paragneiss are considered a gneiss. Therefore, gneiss is the dominant lithology for this particular unit in the model

Vardar Suture Zone(VSZ)

The Vardar suture zone(VSZ) is a remnant of the Vardar ocean which closed in the Late Cretaceous (van Hinsbergen et al., 2005).
It is considered the most internal part of the Hellenidic nappe stack and is partly obducted on top of the Pelagonian Carbonate platform (Menant et al., 2016)
and Continues as the Izmir-Ankara suture in Turkey (Philippon et al., 2014; Menant et al., 2016). It was created by the convergence between Adria and Rhodope and is described as a magmatic arc with 1 to 2 ophiolitic basins and a platform unit (Jolivet and Brun, 2010), but is also described as consisting mostly of serpentinized ophiolite (Philippon et al., 2014). Therefore this unit is prescribed a lithology consisting completely out of serpentinite.

Pelagonia

The Pelagonian Unit is assigned a biogenic sediment chalk lithology consisting of 75% chalcite, because it was originally made of a continental basement with carbonates on top of it (van Hinsbergen et al., 2005). (Mesozoic) carbonate cover with a Jurassic Ophiolite on top of it (Jolivet and Brun, 2010)

Pindos and CBU

The Pindos & Cycladic Blueschist Unit is probably a former oceanic plate/domain which was spreading from the Dinarides to possibly the Lycian basin located in the Taurides (Menant et al., 2016). The Pindos unit probably had an oceanic basement and is described by a greenschist to prehnite metamorphic facies, whereas the Cycladic Blueschist unit has a continental basement, which could represent the passive margin of the Pindos ocean (van Hinsbergen et al., 2005) with Adria. The Pindos suture zone itself probably consists of Triassic-Paleocene limestones and Siliceous sediments covered with Eocene-Oligocene Flysch (Jolivet and Brun, 2010). It is chosen to be mainly basalt, because of its oceanic origin with a fraction of eclogite and schist in it. Basalt was chosen over gabbro because the unit is part of a nappe stack, so it should probably be an off-scraping of the top part of the oceanic plate which is generally basaltic.

Cycladic basement

To correlate units throughout the area, one should come up with valid arguments and observations, because the geological setting of the Aegean offshore area and its surroundings is very complicated. However, constructing an input-model of the main crustal units in this area is hard enough by itself. Therefore, an attempt was made to keep the input model as simple as possible by using the least crustal units possible, for example with the Cycladic basement. In the literature there are often two units which are referred to as either the Menderes massif/Cycladic basement (Jolivet et al., 2013; Menant et al., 2016) and Gavrovo-Tripolitza (van Hinsbergen et al., 2005; Jolivet and Brun, 2010; Menant et al., 2016). From Jolivet et al. (2013) : *"An alternative view was proposed by Jolivet et al. (2004): the basement and cover of the Menderes Massif correlate with the Gavrovo-Tripolitza nappe and its basement."* Therefore, the decision was made to view them as one and the same unit. Jolivet et al. (2013) describe the Menderes Massif to be consisting of a gneissic core with a schist and marble cover. Therefore, the unit is assigned a mixture of gneiss, marble and schist, of which gneiss is the largest part

Migmatite

The cross-sections of for example Jolivet and Brun (2010); Jolivet et al. (2013); Menant et al. (2016) clearly suggest that there is a lot of migmatite present in the lower crust and this is adopted in the input-model. However, putting a constraint to the composition of this unit is rather difficult, because the term migmatite generally just means that the rock is a mixture between igneous and metamorphic rock e.g. (Earle, 2015), which are commonly occurring in the cores of exhumed gneiss domes (Kruckenberg et al., 2011). For example, a distinction can be made between migmatites that are called metatexites, which are defined by gneisses and schists with a foliation surrounding leucosome, and diatexites, which are controlled by granite surrounding enclaves, selvages, and/or crystals (Kruckenberg et al., 2011). Still, these kinds of descriptions leave open space for different interpretations. In the cores of the metamorphic domes in Rhodope, the Menderes massif & Cyclades, migmatites and associated leucogranitic veins and migmatites associated with S-type granites have been described (Brun and Sokoutis, 2007; Menant et al., 2016). At least, the descriptions of the migmatite present in this area reveal that they are granitic to an extent. In terms of metamorphism, migmatite appears after gneiss when it comes to a typical geothermal gradient, see figure 14. Therefore, this unit is assigned a composition of 50 % granite and 50 % gneiss. It would be better to address every location containing a lot of migmatite separately, but since the migmatite layer is treated as 1 more or less continuous layer, this was not done.

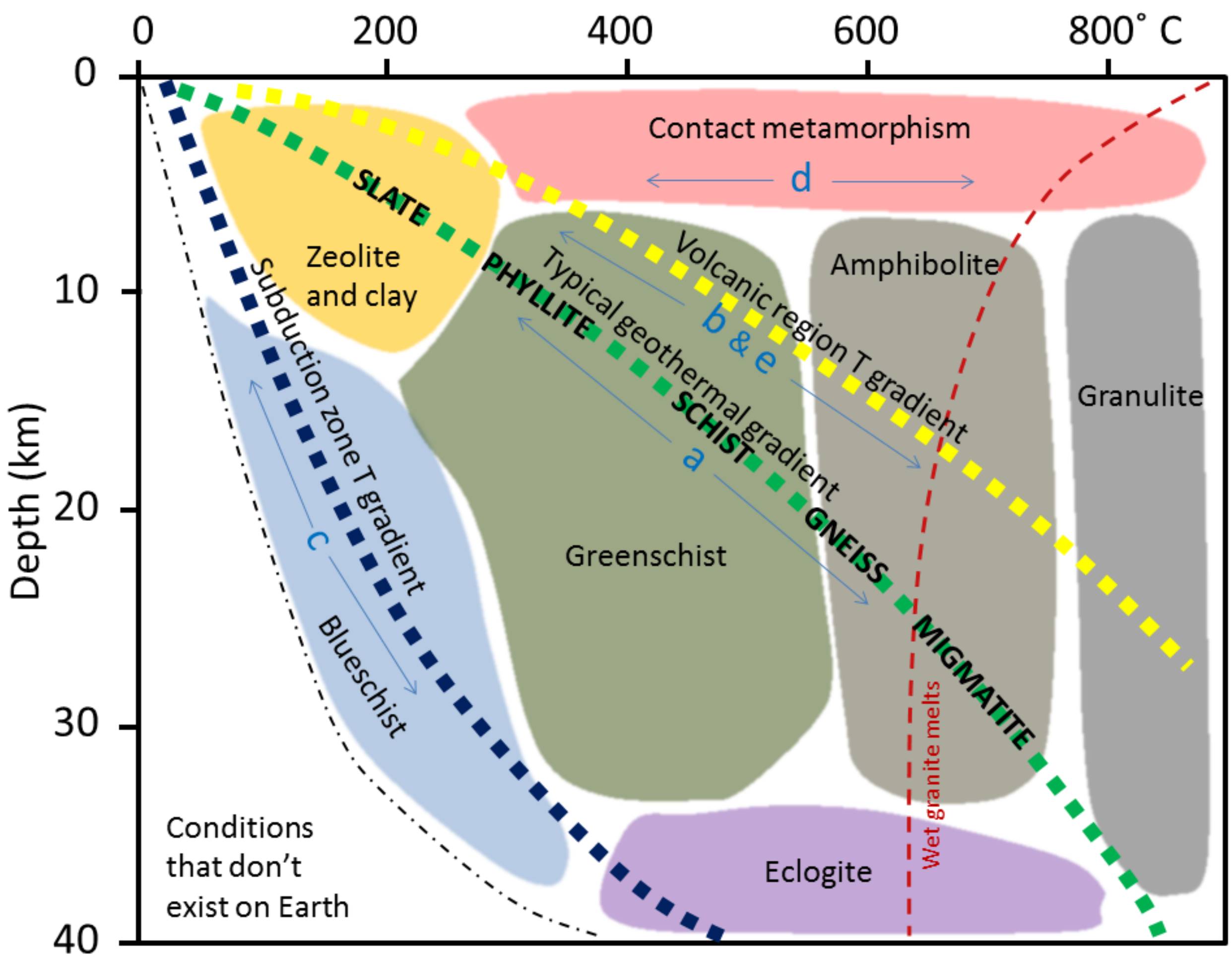

Figure 14: P-T of metamorphic facies, from (Earle, 2015)

2.2.3 Lithospheric mantle

The assumption is made that the lithospheric mantle consists completely out of peridotite, due to a lack of available data, this is based on the lithology used for the thermo-mechanical structure of the European lithosphere (Limberger et al., 2018).

3-D lithospheric geological model

It is interesting to look at the effect of the depth of the (thermal) Lithosphere-Astenosphere Boundary(LAB), which is defined here as the transition between a predominantly conductive lithosphere and a predominantly convective asthenosphere(Limberger et al., 2018).

Different researches show different thicknesses. Therefore, 4 models are made, to test different scenarios:

1. The LAB being directly at the Moho
2. The LAB being 10 km below the Moho
3. The LAB being 50 km below the Moho
4. The LAB being at a depth of 100 km with respect to sea-level

The first and second scenario are based on the crustal structure visualized by (Menant et al., 2016) showing a very thin crust throughout the area of interest. The third is based on a very schematic cross-section shown in the work of (Mitropoulos and Tarney, 1992). The fourth and last scenario is based on (Jolivet and Brun, 2010; Jolivet et al., 2013) where they place the LAB at a depth of 100 km. For all the different scenarios the geometry and composition of the crust will remain the same.

3 Thermal model of the Aegean Sea

The modeling of the temperature distribution was done using the B3t software developed at TNO. The thermal modelling software uses a 1-D approach, before it calculates the 3-D thermal field. The first calculation uses a multi-1D method *basin3dpreprocess* which calculates a 1-D steady state thermal solution for the area. An explanantion of the usage of the software is given in section 3.1.4.

First, a brief description of the important theory is given following Limberger (2018), (section 3.1.1-3.1.3). This is followed by a description of the software and finally a description of the Aegean model, including its geometry, material properties and boundary conditions.

3.1 Theory

3.1.1 Thermal conductivity

1-D conductivity profiles are created as the thermal conductivity is corrected for P- and T-conditions:

$$k(z) = \begin{cases} k_{SED}(z) & 0 \leq z < z_{topUC} \\ k_{UC}(z) & z_{topUC} \leq z < z_{topLC} \\ k_{LC}(z) & z_{topLC} \leq z < z_{topLM} \\ k_{LM}(z) & z_{topLM} \leq z < Z_{LAB} \end{cases} \tag{1}$$

$k_{SED}(z)$, $k_{UC}(z)$, $k_{LC}(z)$ and $k_{LM}(z)$ are the thermal conductivities of the sediments, upper crust, lower crust and lithospheric mantle as a function of depth z in [m], together making up the total thermal conductivity as a function of depth k_z. z_{topUC}, z_{topLC}, z_{topLM} and z_{LAB} are the depths [m] of the top of the upper crust, the top of the lower crust, the top of the lithospheric mantle and the Lithosphere-Asthenosphere Boundary (LAB), respectively.

Each lithotype has a matrix thermal conductivity k_m. These conductivities are corrected for the in situ temperature according to Sekiguchi (1984):

$$k_m(z) = 358 + (1.0227 \cdot k_i^{20} - 1.882) \cdot (\frac{1}{T} - 0.00068) + 1.84 \tag{2}$$

In this equation k_i^{20} denotes the matrix thermal conductivity at room temperature (20 °C) an T denotes the temperature [K]. The conductivities are calculated apart from the temperature-dependent conductivity water, which is assumed to be the pore fluid that resides in the sediments. Additionally, the matrix thermal conductivities of carbonates are corrected for the change in anisotropy due to increasing compaction, from (Hantschel and Kauerauf, 2009). A weighted average of the lithotypes in a sedimentary layer was taken for the bulk density, that depends on the amount of mechanical compaction. All other layers in the crust have fixed densities. Compaction is calculated using Schneiders relationship. Surface porosities for the lithotypes are assigned the values of the depositional porosities from Hantschel and Kauerauf (2009). This, combined with the compaction coefficients is used to calculate the porosity as a function of depth. A bulk matrix conductivity, $k_{bulkmatrix}$, is obtained by taking the harmonic mean of all the matrix thermal conductivities. In the end, the depth-dependent conductivity of the sediments is obtained through the following equation:

$$k_{SED}(z) = k_{bulkmatrix}^{1-\phi} \cdot k_w^{\phi} \tag{3}$$

where k_w is the thermal conductivity of the pore fluid and ϕ the porosity.

The thermal conductivity of the crust is corrected for temperature and pressure using the relations from Chapman (1986), assuming that the effective vertical stress and lithostatic pressure is equal.

$$k_{UC}(z) = k_{iUC}^{0} \cdot \Big(\frac{1 + c \cdot \sigma_v^{'}}{1 + b \cdot T}\Big) \tag{4}$$

$$k_{LC}(z) = k_{iLC}^{0} \cdot \Big(\frac{1 + c \cdot \sigma_v^{'}}{1 + b \cdot T}\Big) \tag{5}$$

In these two equations k_{UC} and k_{LC} denote the thermal conductivities of the upper and lower crust, k_i^0 denotes the thermal conductivity at 0°C and atmospheric pressure. $\sigma_v^{'}$ is the effective vertical stress, T [°C] is the temperature and b [K^{-1}] and c [Pa^{-1}] are constants. The radiative component of the thermal conductivity will play a bigger role than the lattice component of thermal conductivity, when temperatures go up. Therefore the equations of Schatz and Simmons (1972) and Xu et al. (2004) to calculate the depth-dependent conductivity of the lithospheric mantle:

$$k_{LM}(z) = k_{lat}^{25}(T, \sigma_v^{'}) + k_{rad}(T) = \sqrt{\frac{298}{T+273}} \cdot (1 + 0.0032 \cdot \sigma_v^{'}) + 0.368 \cdot 10^{-9} \cdot (T+273)^3 \tag{6}$$

Here k_{LM} denotes the thermal conductivity of the lithospheric mantle, $k_{lat}^{25}(T, \sigma_v^{'})$ denotes the temperature- and pressure dependent lattice component of the thermal conductivity of olivine (Limberger, 2018) at 25 °C and $k_{rad}(T)$ the temperature dependent radiative component of the thermal conductivity. T is the temperature [K] and $\sigma_v^{'}$ the effective lithostatic stress in [GPa]

3.1.2 Radiogenic heat generation

The radiogenic heat generation $A(z)$ $[\mu W m^{-3}]$ in the lithosphere is approached in the same way as the thermal conductivity, except that the values are constant with depth depending on the lithotype:

$$A(z) = \begin{cases} A_{SED}(z) = A_{bulk} & 0 \leq z < z_{topUC} \\ A_{UC}(z) = A_{lithotype} & z_{topUC} \leq z < z_{topLC} \\ A_{LC}(z) = A_{lithotype} & z_{topLC} \leq z < z_{topLM} \\ A_{LM}(z) = 0.02 & z_{topLM} \leq z < z_{LAB} \end{cases} \tag{7}$$

$A_{SED}(z)$, $A_{UC}(z)$, $A_{LC}(z)$ and $A_{LM}(z)$ are the values of the radiogenic heeat genertion of the sediments, upper crust, lower crust and lithospheric mantle respectively, with respect to depth. The heat production of siliclastic lithotypes does increase with depth as the amount of pore fluid becomes relatively smaller due to compaction. There are several factors that can have an effect on shallow surface heat flow measurements from wells, such as paleoclimatic perturbation and groundwater flow. Erosion can lead to overestimations of the heat flow, whereas sedimentation can lead to underestimations (Limberger, 2018).

3.1.3 Surface heat flow and temperature

As mentioned above, the thermal conductivity is temperature-dependent and therefore needs to be corrected. For a start, the temperature is estimated by a multi 1-D steady-state calculation of the heat equation. 1-D surface heat flow is estimated according to the following equation, from (Limberger, 2018):

$$
\begin{aligned}
Q_0 \approx \Bigg[& T_{LAB} - T_0 + \\
& \frac{1}{2} \cdot \left(\bar{A}_{SED} \cdot \frac{\Delta z_{SED}^2}{\bar{k}_{SED}} + \bar{A}_{UC} \cdot \frac{\Delta z_{LC}^2}{\bar{k}_{UC}} + \bar{A}_{LC} \cdot \frac{\Delta z_{LC}^2}{\bar{k}_{LC}} + \bar{A}_{LM} \cdot \frac{\Delta z_{LM}^2}{\bar{k}_{LM}} \right) + \\
& \bar{A}_{SED} \cdot \Delta z_{SED} \cdot \frac{\Delta z_{UC}}{\bar{k}_{UC}} + \left(\bar{A}_{SED} \cdot \Delta z_{SED} + \bar{A}_{UC} \cdot \Delta z_{UC} \right) \cdot \frac{\Delta z_{LC}}{\bar{k}_{LC}} + \\
& \left(\bar{A}_{SED} \cdot \Delta z_{SED} + \bar{A}_{UC} \cdot \Delta z_{UC} + \bar{A}_{LC} \cdot \Delta z_{LC} \right) \cdot \frac{\Delta z_{LM}}{\bar{k}_{LM}} \Bigg] \Bigg/ \\
& \left[\frac{\Delta z_{SED}}{\bar{k}_{SED}} + \frac{\Delta z_{UC}}{\bar{k}_{UC}} + \frac{\Delta z_{LC}}{\bar{k}_{LC}} + \frac{\Delta z_{LM}}{\bar{k}_{LM}} \right]
\end{aligned} \tag{8}
$$

Here, Q_0 is the surface heat flow $[Wm^{-2}]$, T_{LAB} is the temperature at the Lithospere-Asthenosphere Boundary $[°C]$ and T_0 the temperature at the surface. The thickness of each layer is denoted by Δz [m] and the averaged thermal conductivity and radiogenic heat production are doneted by $\bar{k}$ and $\bar{A}$. Eventually, the temperature at each layer is calculated with the calculated surface heat flow Q_0, the calculated radiogenic heat production $A(z)$ and the thermal conductivity that is corrected using the the initial temperature, according to the following equation:

$$T(z) = T_0 + \int_0^z \frac{Q(\zeta)}{k(\zeta)} d\zeta \tag{9}$$

To get the heatflow as a function of depth $Q(z)$, the heat flow is extrapolated downward by subtracting the integral of the radiogenic heat production from the surface heat flow between the surface and a depth z, according to the following equation:

$$Q(z) = Q_0 - \int_0^z A(\zeta) d\zeta \tag{10}$$

In the end, a 3-D thermal model can be created, by a finite-difference approximation, using the conductive heat equation:

$$\rho C_t \frac{\partial T}{\partial t} = \nabla \cdot (k_t \nabla T) + A \tag{11}$$

Because the model assumes a steady-state approach, the left-hand side of this equation is set to zero. T is the temperature in [$^{\circ}C$ or K], t is time in [s], ρ is the density in [kgm^{-3}], C_t is the specific heat capacity in [$Jkg^{-1}K^{-1}$], k_t the thermal conductivity in [$Wm^{-1}K^{-1}$], and A the radiogenic heat production in [Wm^{-3}].

The model is created with a fixed volume, which is discretized horizontally and vertically. The Preconditioned Conjugate Gradient method (PCG) is then used to solve the set of linear equations resulting from the discretization of the volume.

3.1.4 B3t

Due to a lack of applicable data, the software wasn't used to its full extent. Therefore, only the functions that were applied, which are based on the theory discussed above, are discussed in this section. Firstly, it is important that the files containing 3-D data on the crustal units, and the outline that make up the area of interest, are according to a meter coordinate system and are exported as ASCII-grids.

basin3dpreprocess

The first calculation uses a multi-1D method *basin3dpreprocess* which calculates a 1-D steady state thermal solution for the area. The voxet that is created by *basin3dpreprocess* can later be used as input for the calculation of a 3-D thermal field.

In a graphical user interface you delimit the area of interest by typing in *xmin, xmax, ymin* and *ymax* in meters [m]. With *nx* and *ny* you prescribe the amount of gridcells. Also you can define the depth down to which the model is in high resolution at *high res depth* and the spacing belong the the high resolution part at *high res DZ*. Similarly, the low resolution part is defined at *low res total depth* and *low res DZ*. In the *model setup* section you can put in 3 files; a file that indicates which cells are used for the calculation of the model (cells with nodata-values are excluded), a file that contains information on rock properties & a file in which the succession of the grids is defined The last file named contains a table, consisting of a maximum of eight columns, where, among other things, the parameters of each unit are defined:

1. Here a number defines the location of each unit. Negative numbers denote parts of the crust and lithospheric mantle, the lower the number, the deeper the unit e.g. -1 is upper crust, -2 lower crust etc.. Positive numbers denote sediments, the lower the number, the younger the sedimentary layer.

2. The ASCII-files are listed corresponding with the numbers of column 1

3. Defines whether the input of column 2 is in terms of elevation, true vertical depth or thickness

4. Not used in this model

5. This either contains one thermal conductivity value or in information about the composition of the lithologies and their proportions. For example, 50_IRGranite_50_MRGneiss represents a mixture of 50 percent granite and 50 percent gneiss.

6. Heat generation, sub-lithotypes for negative units (column 1) or a burial anomaly for sediments

7. Shrink distance that reduces the extent of the grid from the sides

8. Extrapolate distance that extends the grid from the sides

Furthermore, there is a section on temperature parameters where one can insert different things such as a gradient and boundary conditions. Those can be inserted by filling in a value or a grid, for example a depth value or grid. At least 2 BCs are needed. namely the surface temperature and a temperature or heatflow at a specific depth.

basin3dcalculate

In the graphic user interface one inserts an output-voxet obtained with *basin3dpreprocess*. This voxet contains all the a priori information on the parameters that are used for the 3-D calculation. The calculation needs similar to *basin3dpreprocess* 2 BCs, a surface temperature and a temperature or heat flow at the base.

The model can also be calibrated with for example temperature observations from wells, which need to be in in a .csv-file. Unfortunately, in this research, there was no acces to such data. Therefore, no calibration took place.

3.2 Constraints

3.2.1 Resolution

The surface grid used in this research contains 11484 cells, 99 cells in the x-direction and 166 cells in the y-direction, with a cellsize of 5000 times 5000 meters. The total depth of the model was set to 100000 meters with a cell-spacing of 400 meters, containing 250 cells in the z-direction.

3.2.2 Boundary Conditions

All the models were made with the same basal boundary conditions, but with the (thermal) LAB at different depths. A uniform surface (seafloor) temperature of 10 °C at the top, and a temperature of 1330 °C at the bottom (LAB). The thermal modeling was done for an offshore region. Generally, the bottom of oceans and seas have lower temperatures than 10 °C, but since this is a rather shallow sea, see fig. 15, the surface temperature was assumed to be 10 °C throughout the area.

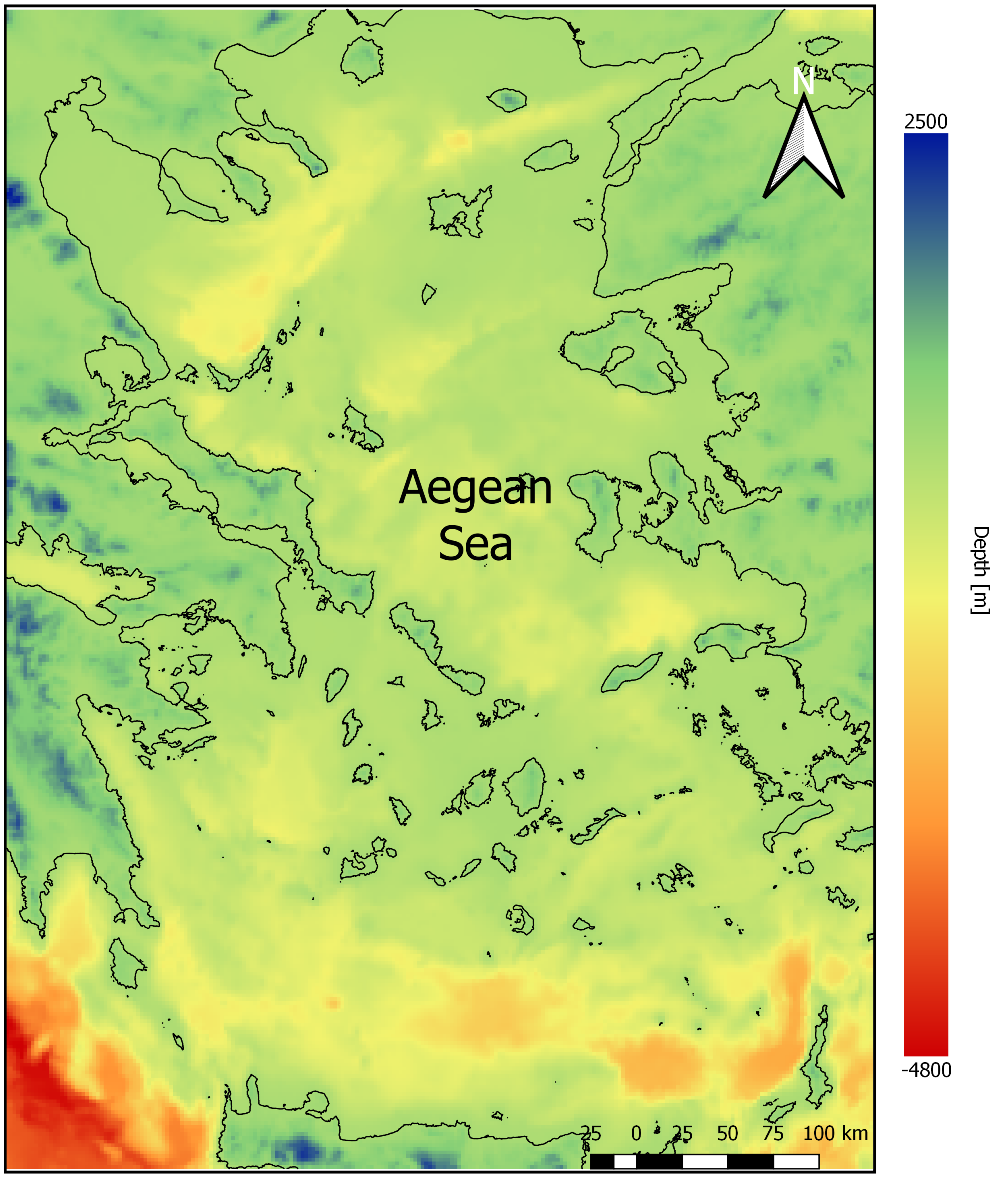

Figure 15: Elevation map of the Aegean Sea, from Amante and Eakins (2009)

3.3 Thermal Data

Table 2 and table 1 show the main crustal units that were used in the model, what their lithologies , their average conductivities and radiogenic heat generation are. Note that these data are based on literature mentioned in sections 2.2.1 and 2.2.2 and not on real measurements.

Table 3 shows a list of relevant surface heatflow measurements, and their corresponding names and coordinates, taken from the *Atlas of Geothermal resources in Europe*, by Hurter and Haenel (2002), for comparison with the surface heatflow maps of the models. The locations were chosen so that there was a measurement for validation in every unit of the crust, see fig. 18.

Table 1: Sedimentary basins, including the lithotypes comprising the sediments, described in section 2.2.1. The listed vertical conductivity and radiogenic heat generation values are surface values and vary with depth, from Hantschel and Kauerauf (2009).

Unit	Lithotype	kz $[Wm^{-1}K^{-1}]$	Porosity ϕ [0-1]	A [μW/m^3]	Max thickness [m]
Thermaikos Basin	27 % Sandstone; clay-rich, 25 % Limestone; typical, organic-rich, 43 % Conglomerate; typical, 5 % Coal; pure	1.30	0.40	0.61	2200
NAT Basin	48 % Sandstone; clay-rich, 19 % Salt , 33 % Conglomerate; typical	1.89	0.29	0.52	2200
Northern Skyros Basin	44 % Sandstone; clay-rich, 25 % Sandstone; typical , 31 % Conglomerate; typical	1.66	0.37	0.58	2000
Ikaria Basin	38 % Sandstone; clay-rich, 21 % Sandstone; typical , 41 % Conglomerate; typical	1.64	0.36	0.58	1500
Cretan Basin	91 % Marl, 9 % Gypsum	1.11	0.46	0.54	4000

Table 2: Crustal units, including the lithotypes described in section 2.2.2. The listed vertical conductivity and radiogenic heat generation values are surface values and vary with depth.

Unit	Lithotype	kz $[Wm^{-1}K^{-1}]$	Porosity ϕ [0-1]	A [μW/m^3]
Rhodope	75 % Gneiss, 15 % Marble, 5 % Schist, 5 % Amphibolite	2.75	0	2.02
Vardar	100 % Serpentinite	2.63	0	0.01
Pelagonia	100 % Chalk (with 75 % calcite content)	0.96	0.67	0.2
Pindos & CBU	90 % Basalt (normal), 5 % Schist, 5 % Eclogite	1.88	0	0.55
Cycladic Basement	80 % Gneiss, 10 % Schist, 10 % Marble	2.77	0	2.18
Migmatite	50 % Granite (150 My old), 50 % Gneiss	2.69	0	2.91
Lithospheric mantle	100 % peridotite	4.13 (at 25 °C)	0	0.02

Table 3: Chosen well locations, shown in figure 16, from (Hurter and Haenel, 2002)

No. Location	Heat Flow $[mWm^{-2}]$	X	Y
11 Aegean Sea	90	863008.2473	4464496.623
12 Aegean Sea	69	813489.3895	4458471.99
16 Aegean Sea	104	795348.5626	4415177.089
24 Anemorahi 2	58	941146.5201	4362744.679
26 Aegean Sea	75	885820.4808	4318898.354
29 Aegean Sea	110	888692.9745	4259831.991
35 G-25 Samos	61	1008888.259	4187859.101
41 Sea of Crete	77	870099.4644	3984552.565

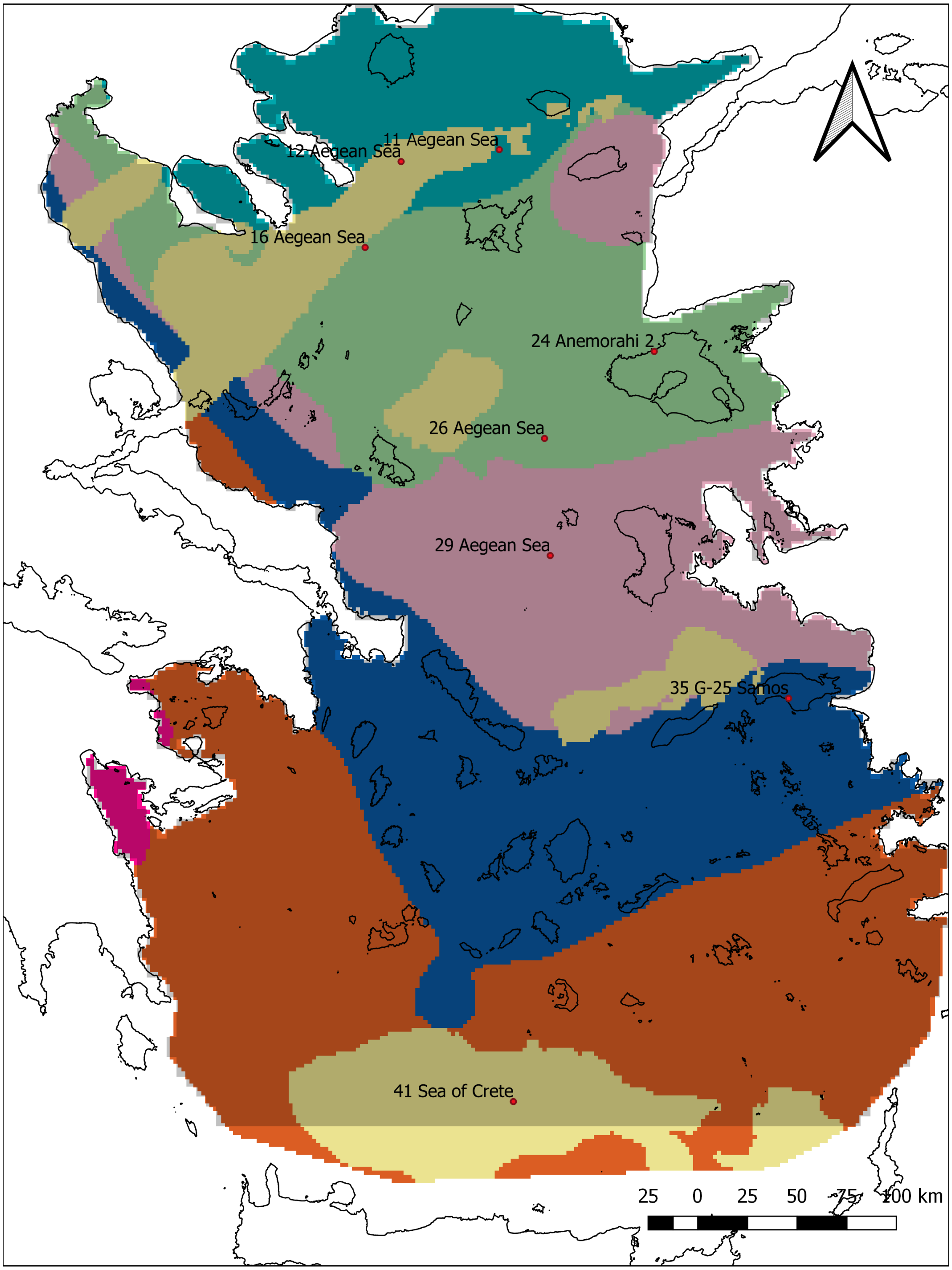

Figure 16: Locations of the wells that are listed in table 3 and are used for the plots of fig. 19 and 21

3.4 Thermal Model

Figure 17: Horizontal depth slices of the four thermal models

(a) 1000 m

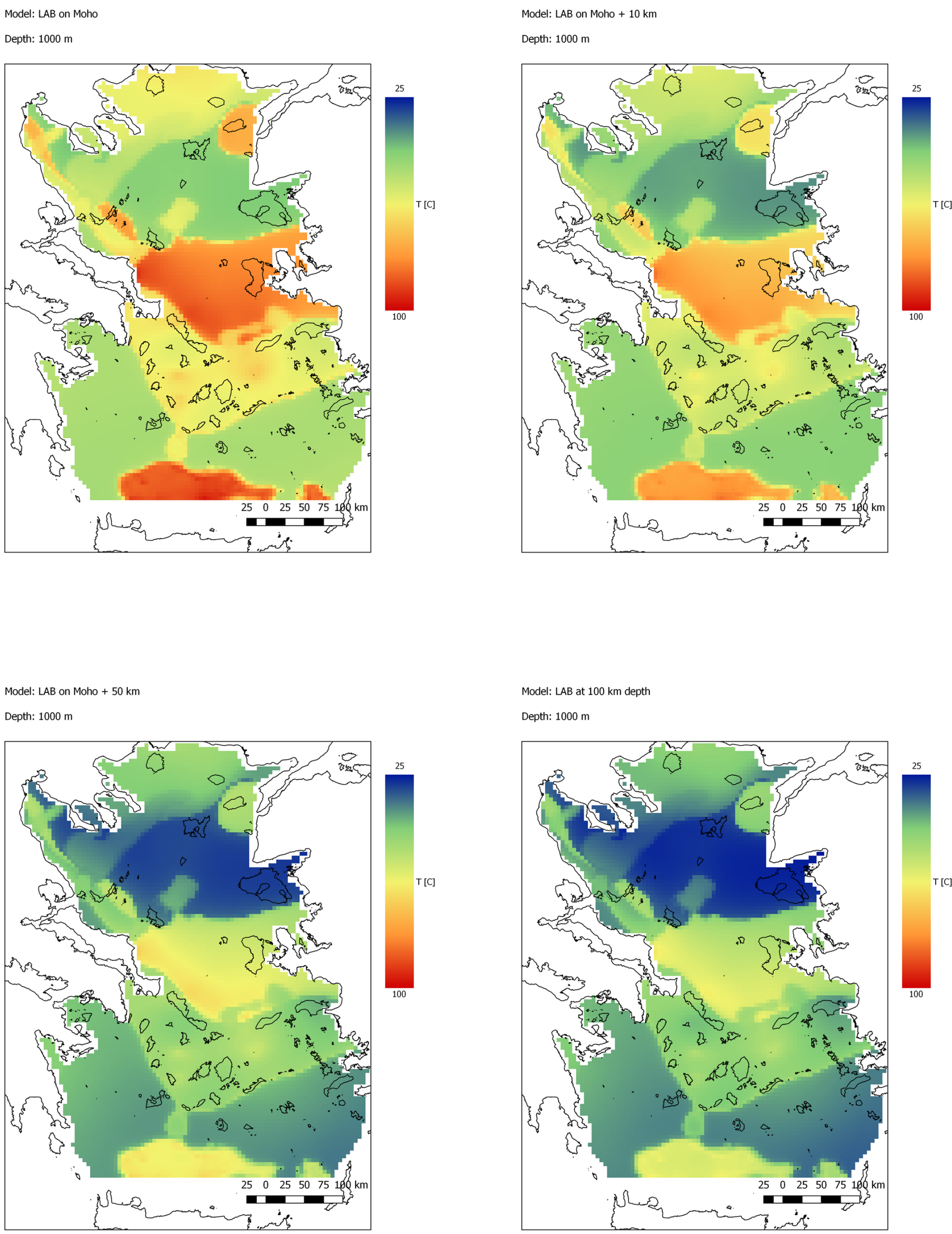

Figure 17: ctd

(b) 2000 m

Model: LAB on Moho

Depth: 2000 m

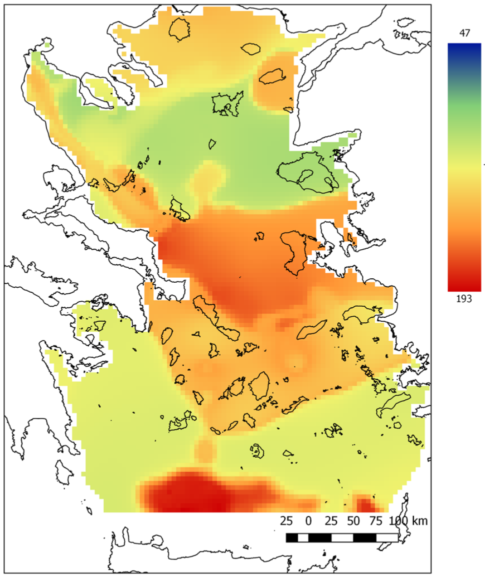

Model: LAB on Moho + 10 km

Depth: 2000 m

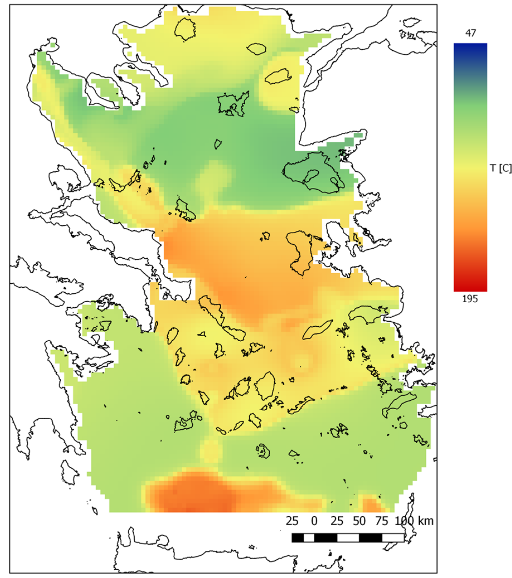

Model: LAB on Moho + 50 km

Depth: 2000 m

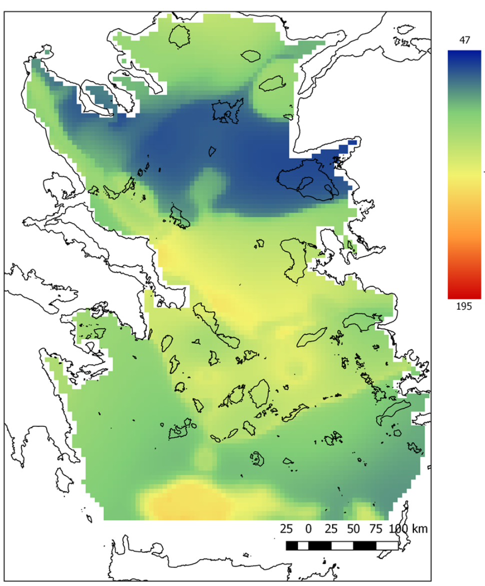

Model: LAB at 100 km depth

Depth: 2000 m

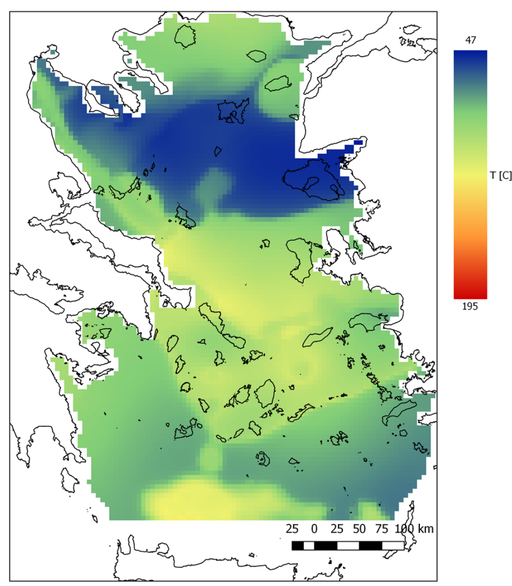

Figure 17: ctd

(c) 3000 m

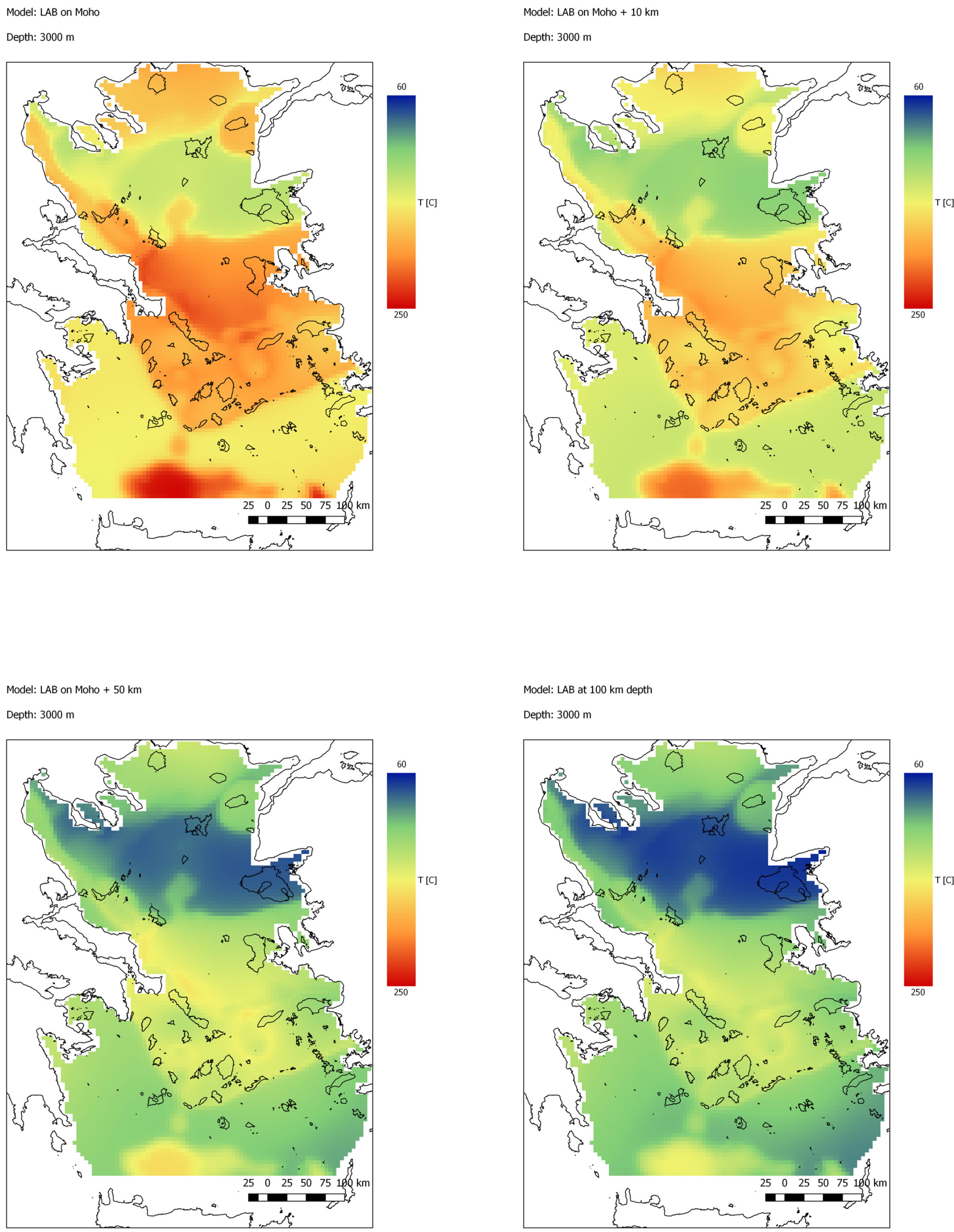

Figure 17: ctd

(d) 4000 m

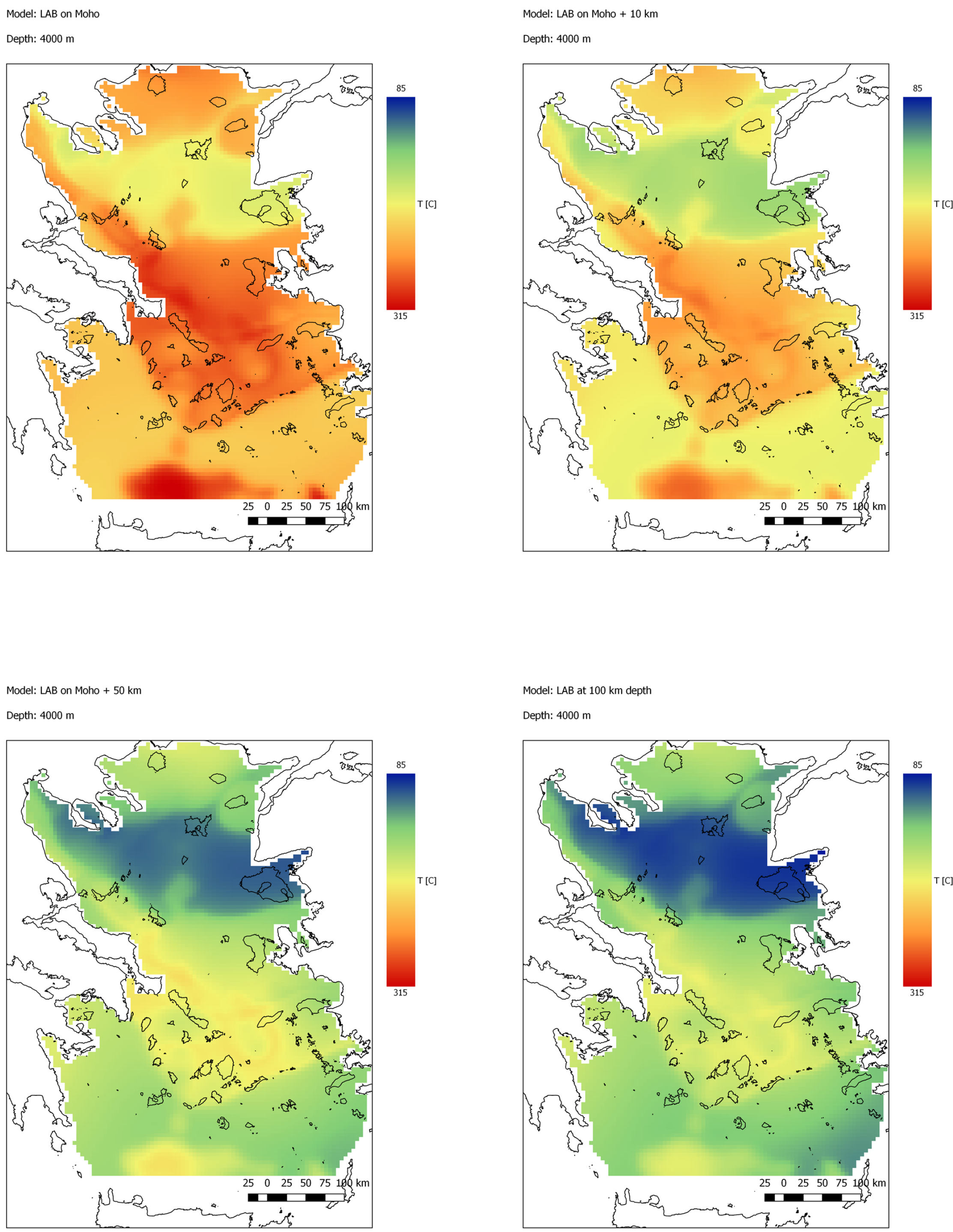

Figure 17: ctd

(e) 5000 m

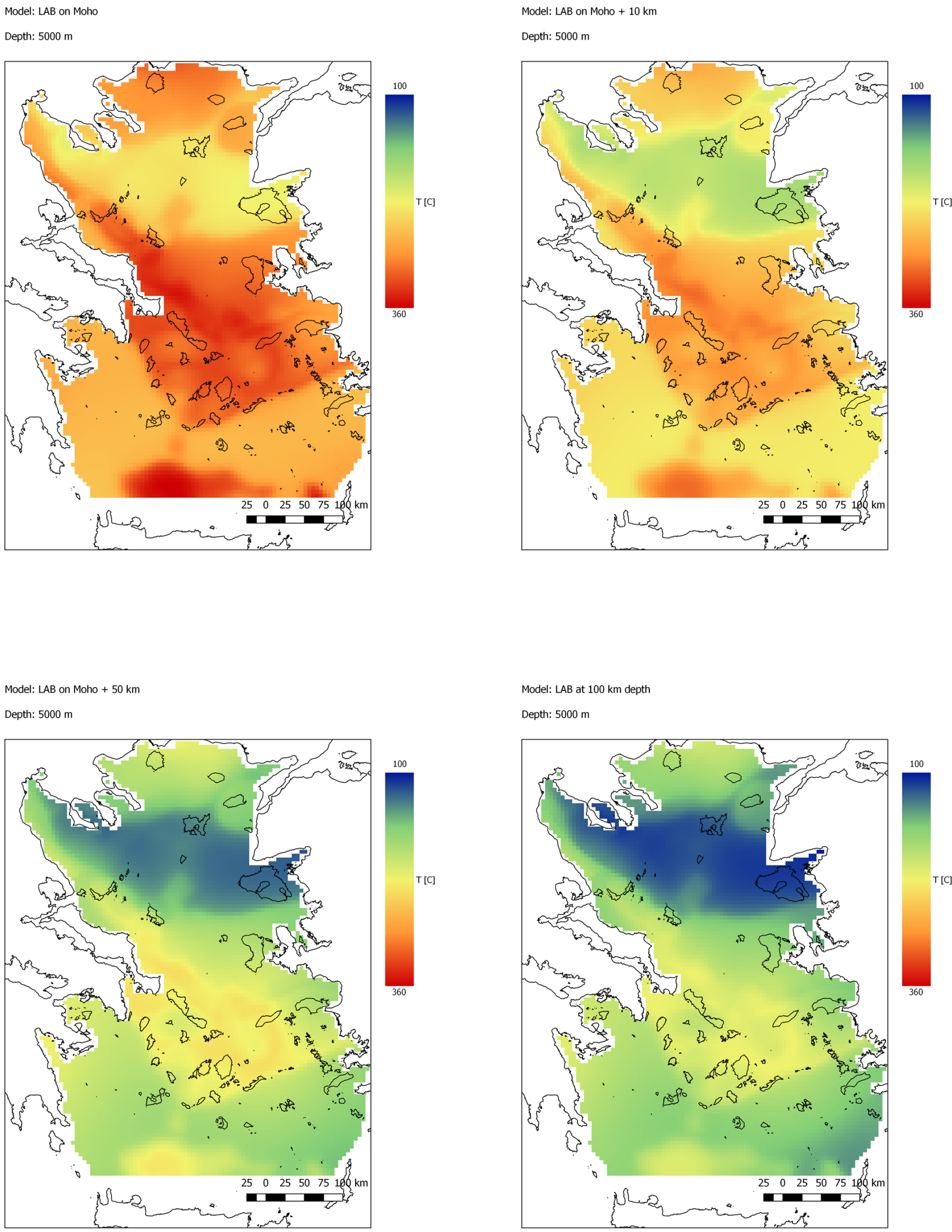

Figure 17: ctd

(f) 8000 m

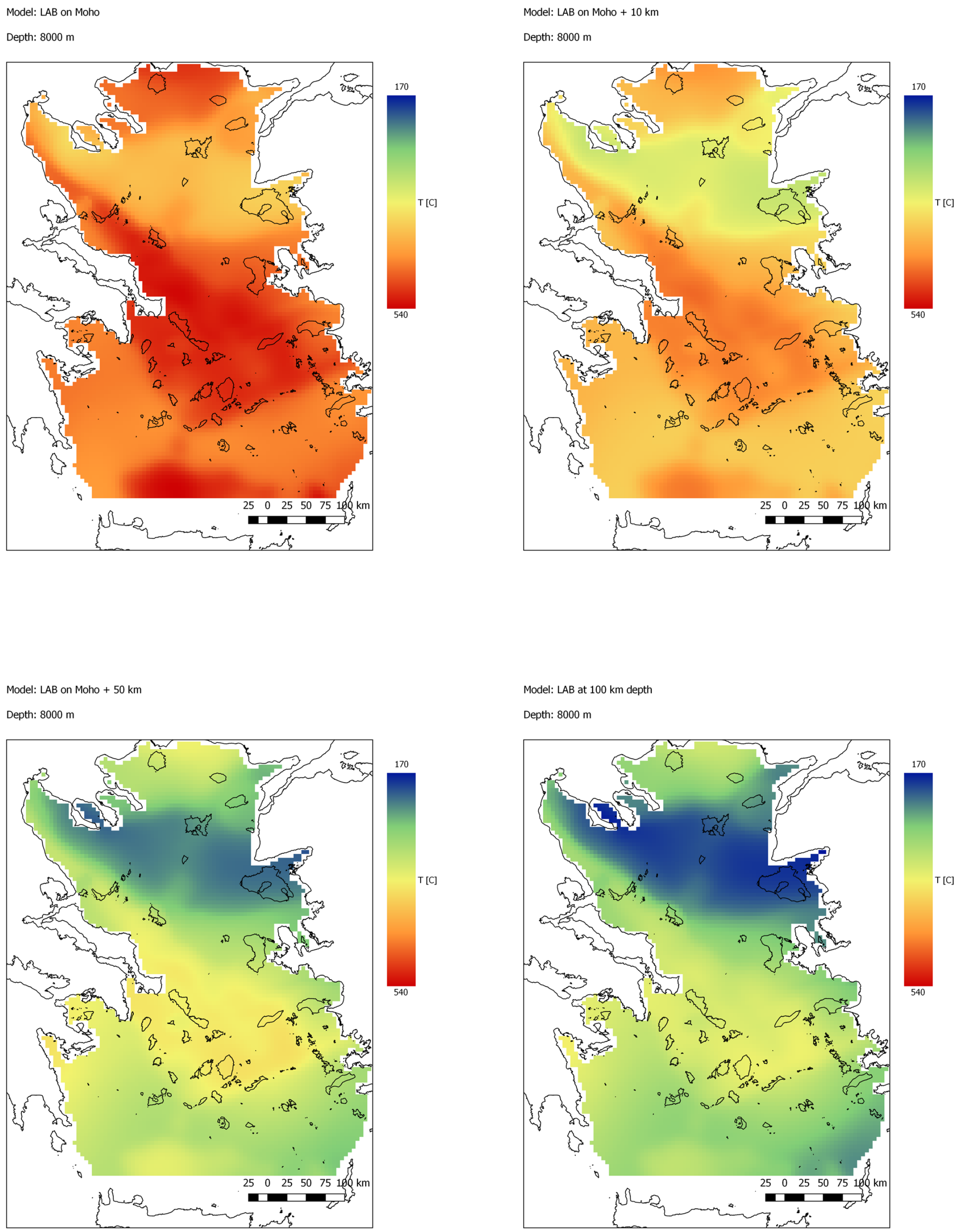

Figure 17: ctd

(g) 10000 m

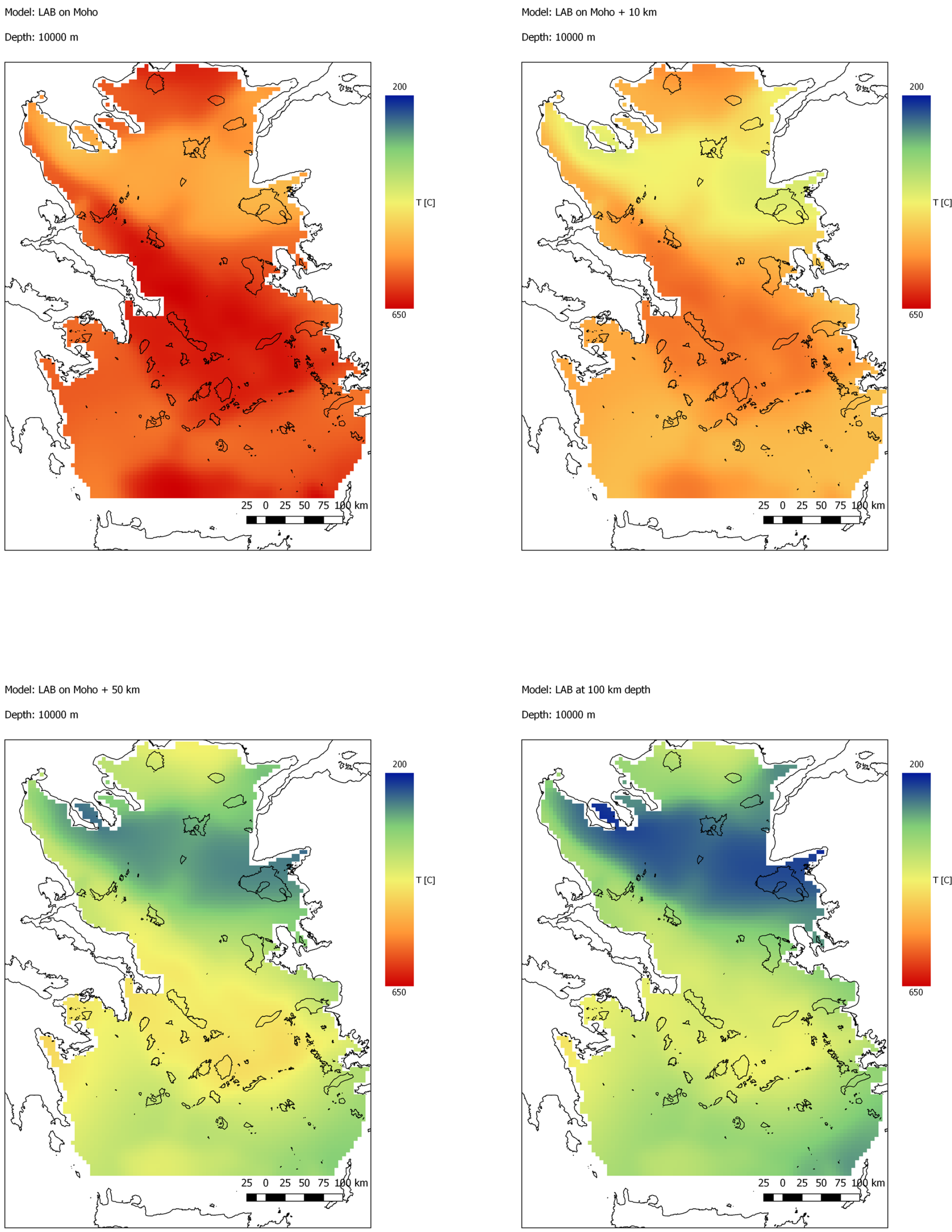

Figure 17: ctd

(h) 15000 m

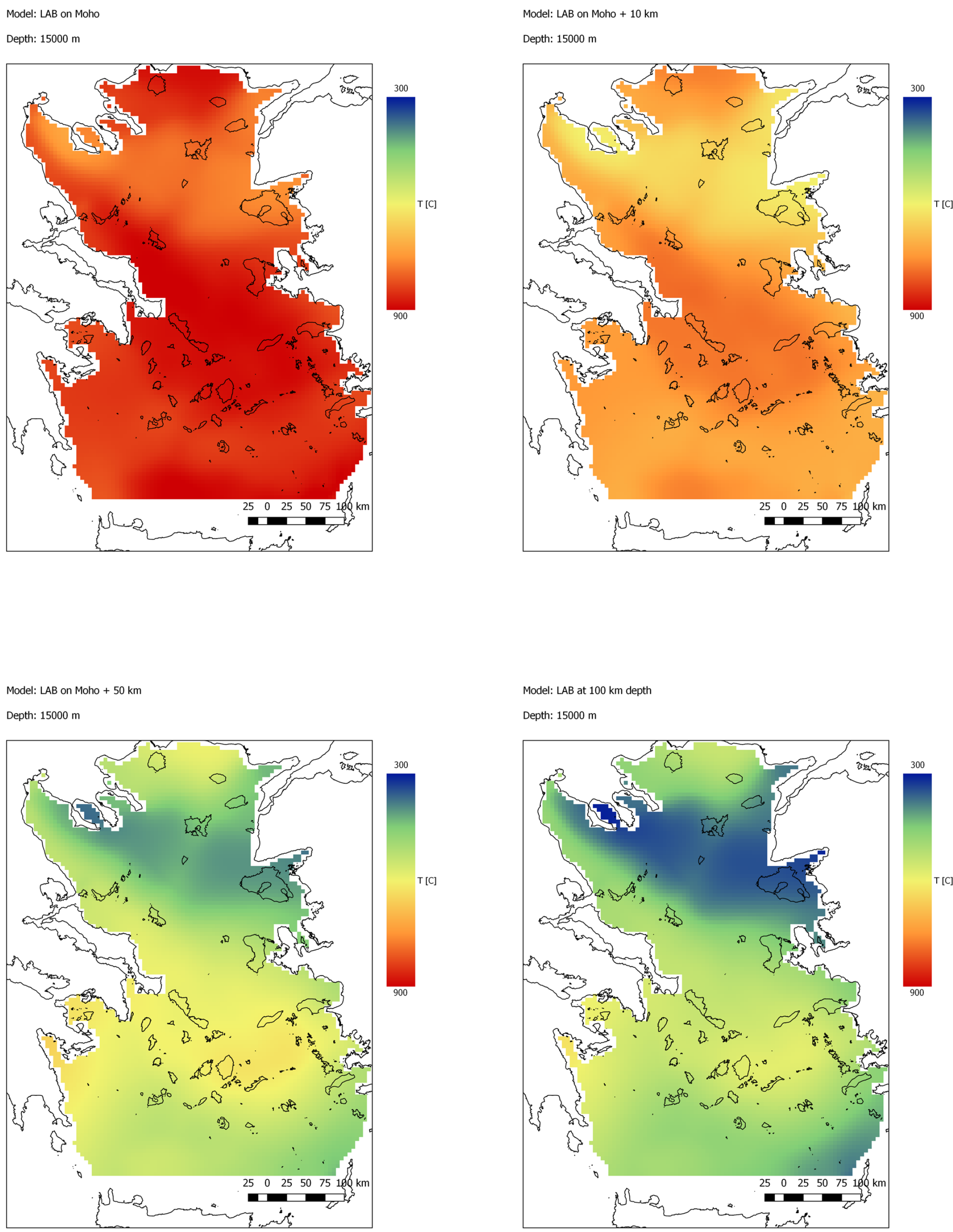

Figure 17: ctd

(i) 20000 m

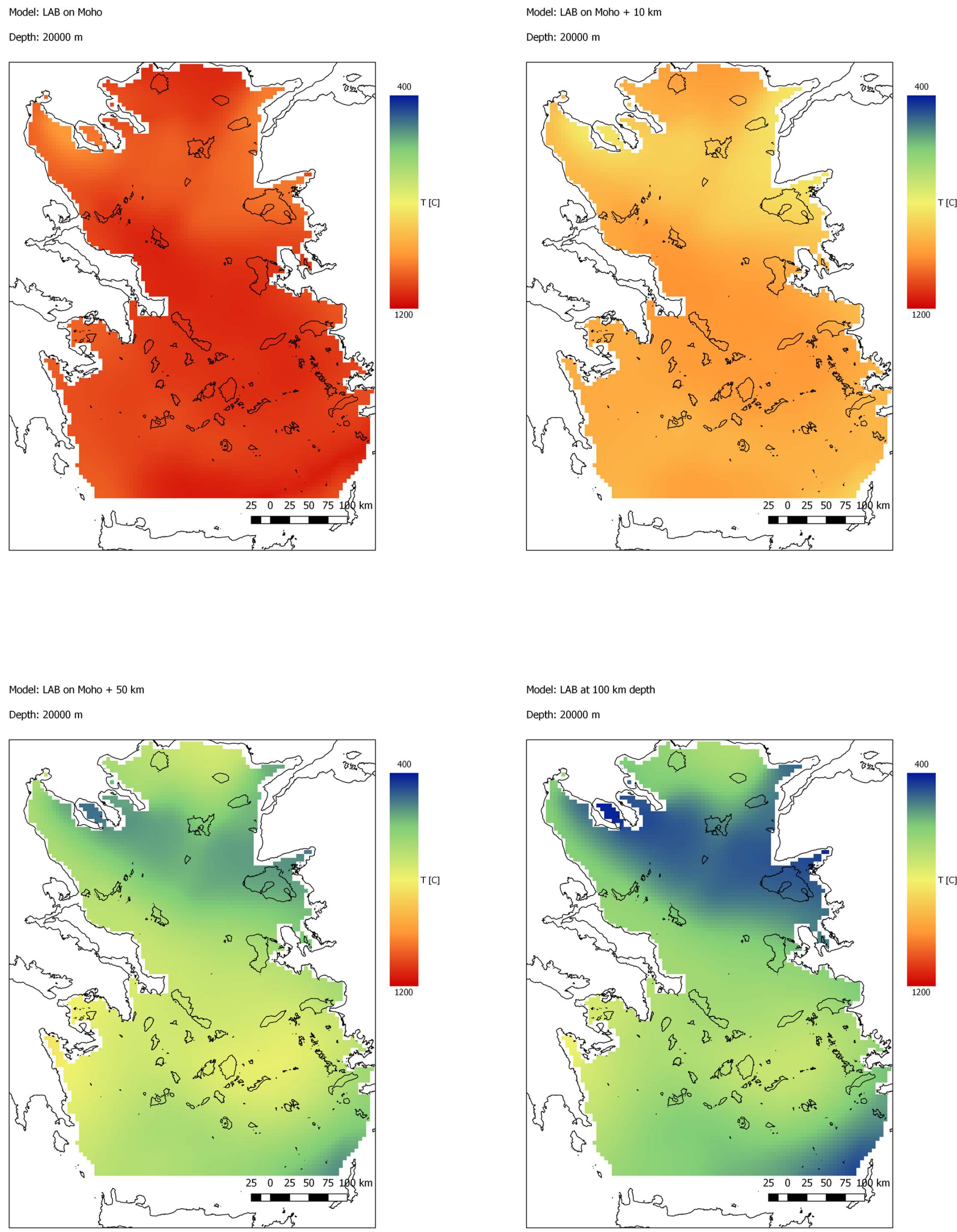

Figure 17: ctd

(j) 25000 m

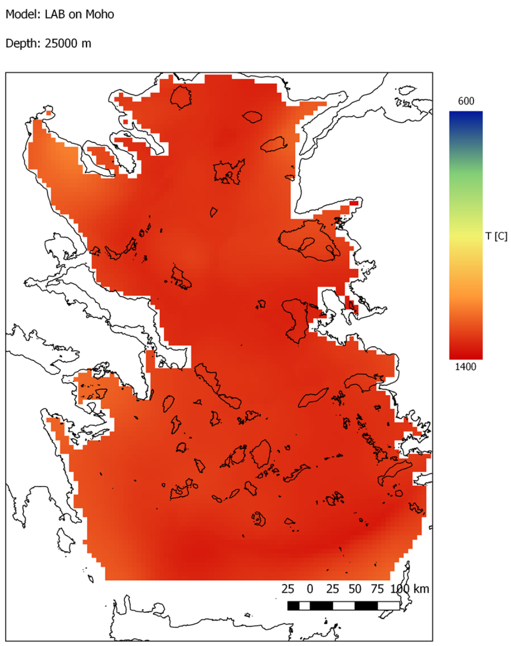

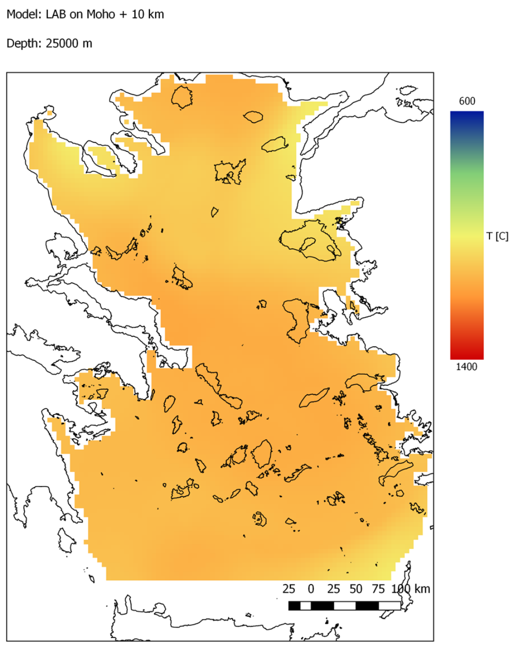

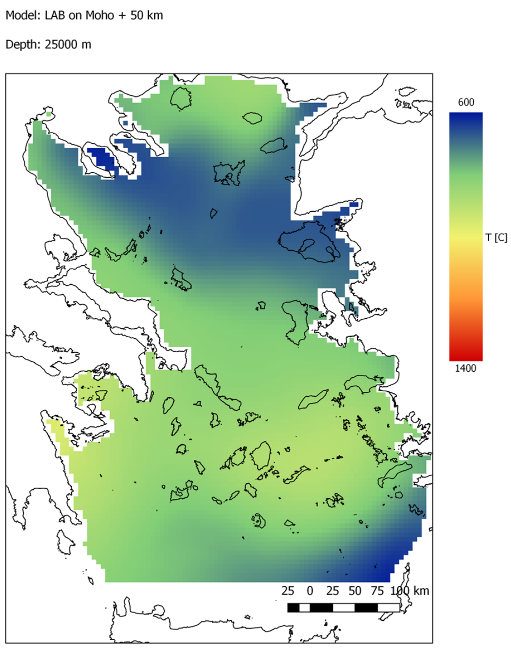

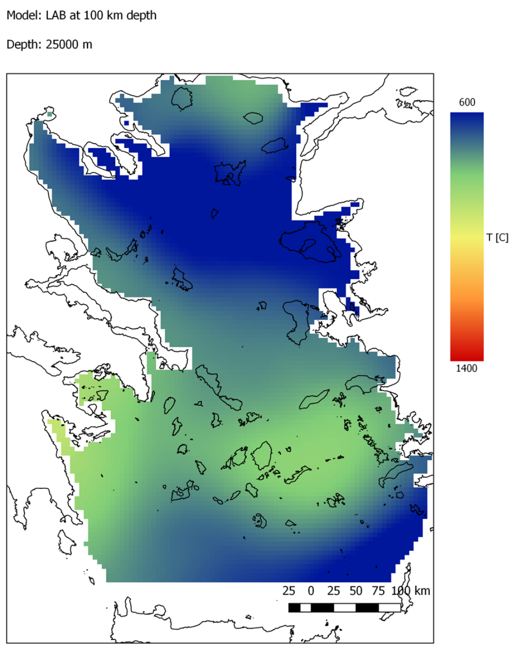

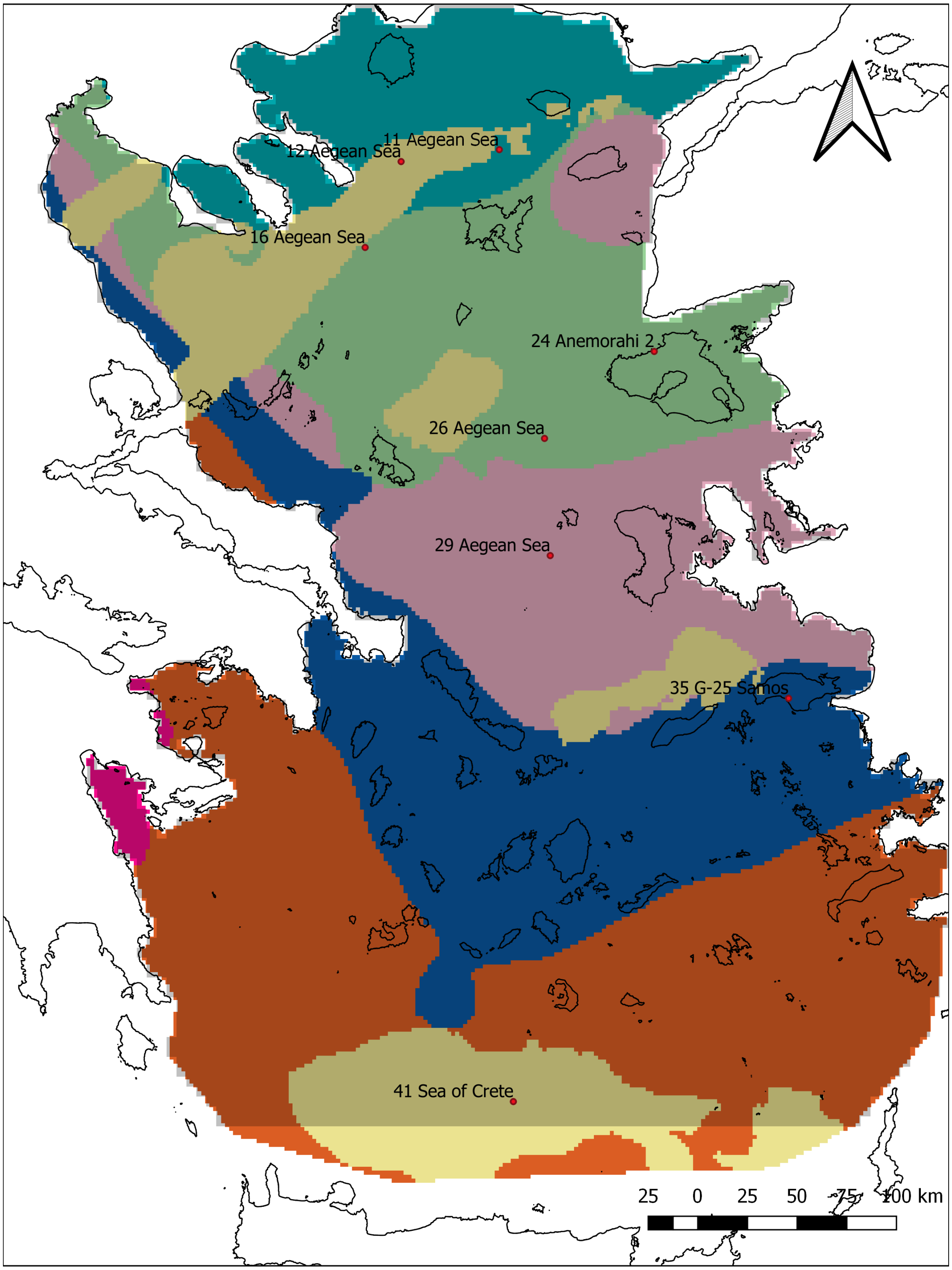

Figure 18: Locations of the wells that are listed in table 3 and are used for the plots of fig. 19 and 21

Fig. 17 represents 4 models of the temperature distribution in the Aegean offshore area with maps at different depths between 1000 m and 25000 m. All the models use the same approach, assuming that there are steady-state conditions. Therefore, the difference between the models lies in the depth of the LAB. Furthermore, transient geological processes have been neglected in the modeling. Temperature-depth maps presented in fig. 17 are shown in the following order; model 1 in the top-left, model 2 in the top-right, model 3 in the bottom-left and model 4 in the bottom right. To compare the models, they are presented using the same temperature scale depending on the depth of the map.

In the shallower parts e.g. fig. 17a, 17b, 17c, 17d and 17e there are abrupt temperature changes visible, generally in accordance with the surface maps of the sedimentary basins and crustal units, see fig. 7 & 12. The lateral temperature distribution becomes gradually smoother with depth and abrupt boundaries are not present anymore (with the used temperature scales) e.g. fig. 17f, 17g, 17h, 17i and 17j. However, the models presented here suggest that a lithosphere with a deeper LAB reaches a uniform lateral temperature distribution more gradually than a lithosphere with a shallow LAB. This can be seen when comparing the models at great depths such as 20000 m and 25000 m, e.g. fig. 17i & 17j.

In the north is a region (Rhodope), which shows relatively intermediate temperatures. More to the south, there is one of the colder areas (Vardar). Further south, in the central Aegean one of the hottest parts is located (Pelagonia). Reaching the Cyclades, an area of relative intermediate temperatures (Pindos) is shown. South of the Cyclades, another relatively cold area (Cycladic basement) is present, before reaching the outermost southern part of the area where the last of the relative hottest areas (Cretan Basin) is located. In the shallower maps, regarding the locations where the basins surface, the temperature is higher than of its surroundings.

In general, the models with a shallower the LAB show higher temperatures throughout lithosphere.

Fig. 19 shows 1-D plots of the temperature and vertical conductivity of the 4 models with respect to depth, at certain wells locations. The heat generation with respect to depth is also included, this is the same for all the models.
The vertical heat generation differs from location to location, see fig. 19. Except at wells 11 and 12, the heat generation increases with depth via sharp inflections to a certain depth where it quickly goes to zero.

(Wells 11 Aegean Sea, 12 Aegean Sea (and 16 Aegean Sea,) see fig. 18 and 19 are all located in the north of the area. 11 and 12 are both located in the region of the Rhodope crustal unit, although 12 is located within the sediments of the Northern Aegean Trough Basin. 16 is already located in the region of the Vardar crustal unit. The heat generation profile at the surface of well 11 is higher than at well 12. Deeper into the lithosphere, the heat generation is more or less the same at both locations. Even further down, the profiles follow the same trend, although the depth of the points of inflection of the profile differs.)

Regarding the temperature profiles, see fig. 19, what most important to note is that the four models have different temperature gradients. The highest gradient belongs to model 1 decreasing to the lowest belonging to model 4 at every location. The temperature gradients tend to have an inflection point at around the same depth as where the heat generation abruptly goes to 0, from that depth the gradient becomes smaller. For model 1 this is not always visible as its profile sometimes runs out of the plotting area before it reaches that depth, for example in the plots of locations; 11, 24, 26 & 35.

Thermal conductivity profiles for the four models are visualized in fig. 19 by the blue coloured lines. The highest conductivity curves are shown by model 1 and the lowest by model 4. All the model profiles have large increase at the same depth as where the radiogenic heat production has a large decrease, at every location. At the locations of wells 11, 12, 29 and 41 and increase followed by a decrease with depth can be noted before reaching the depth of the large increase. At location 16, 24 and 26 the profiles look similar, although there are some wiggles visible in the curves of location 16 and 26. At location 35 the profiles follow an almost vertical path to the depth of the increase.

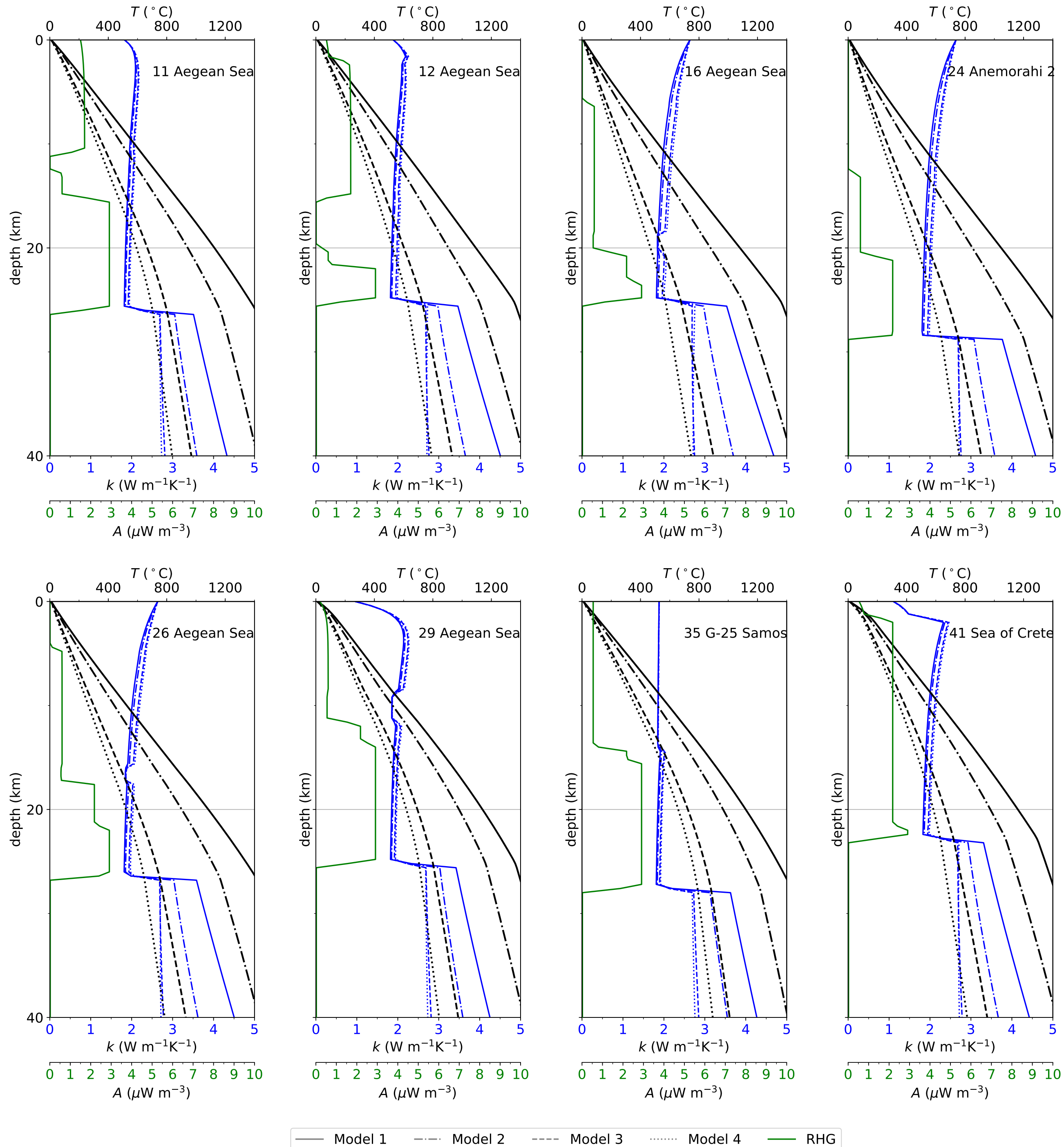

Figure 19: 1-D depth profiles of temperature, conductivity and heat production at 8 different locations (positions indicated in fig. 18)

Figure 20: Surface heat flow maps of the 4 thermal models with the available heat flow measurements. Note that the numbers an colour of each dot denote the heat flow in $[mWm^{-2}]$, from *The Atlas of Geothermal resources in Europe* by (Hurter and Haenel, 2002), of which a few are listed in table 3

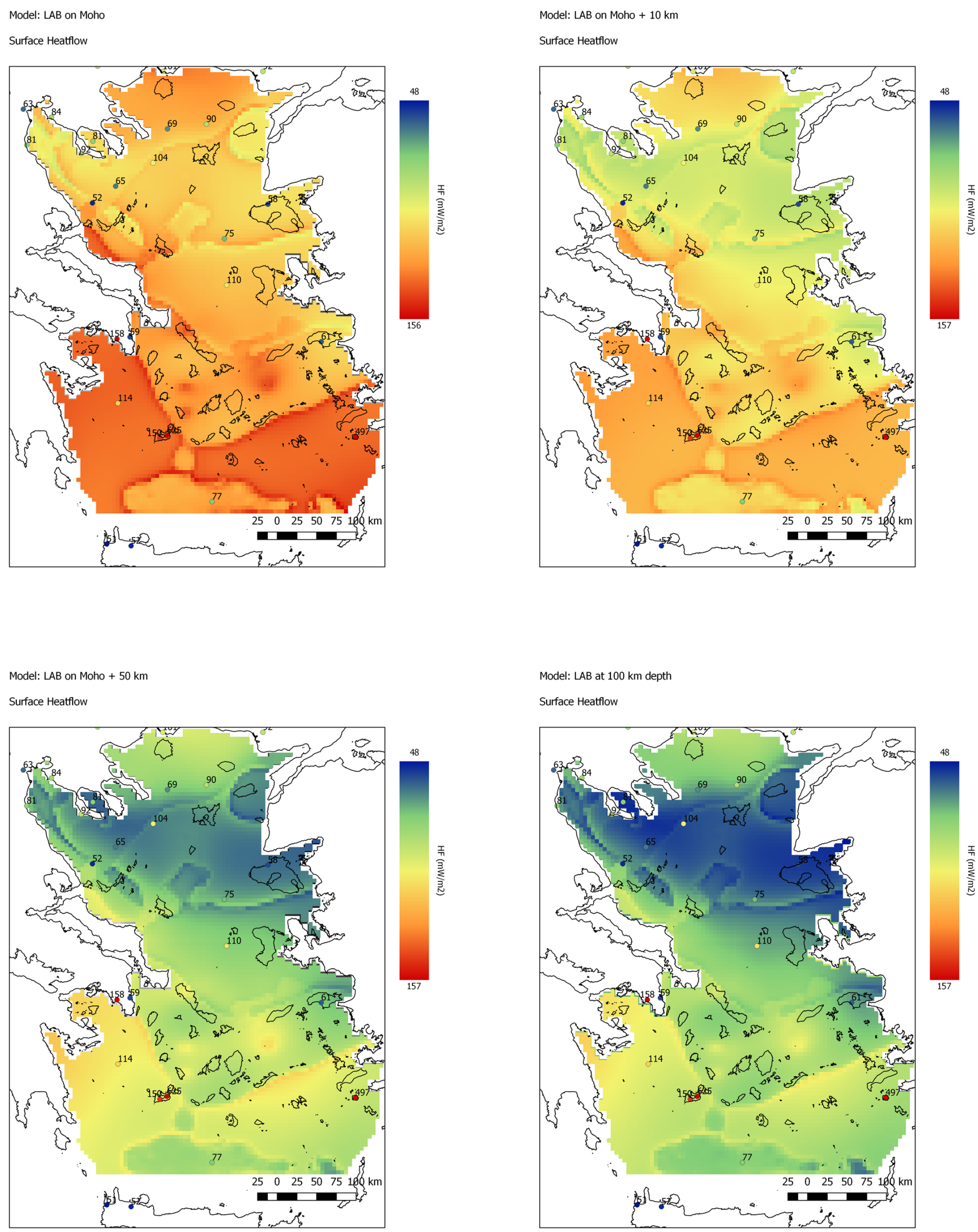

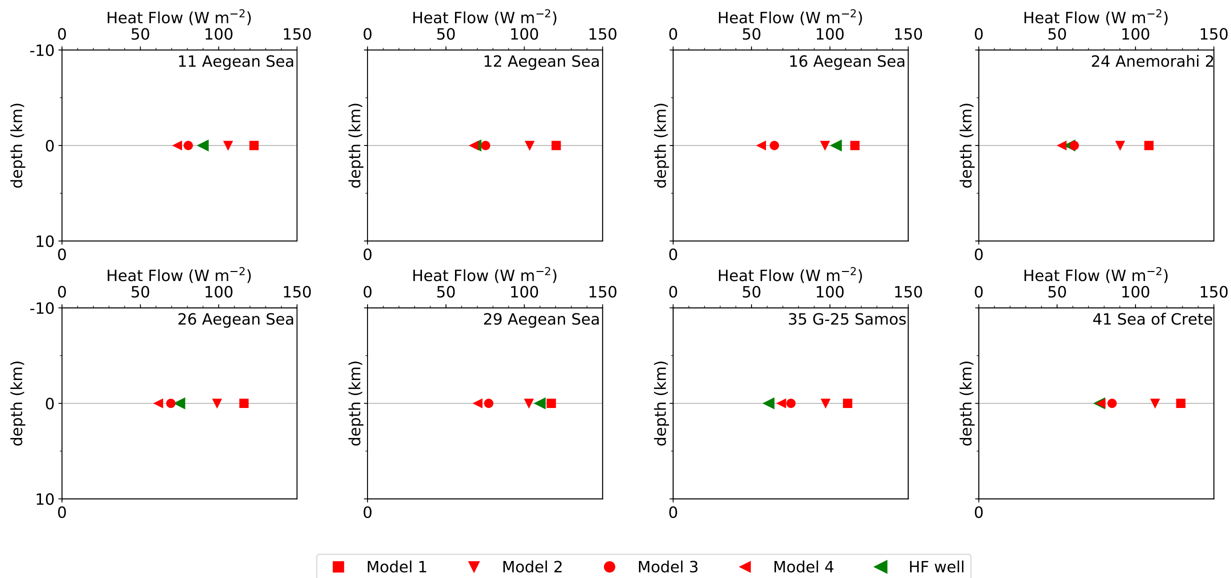

Figure 21: Surface heat flow of the 4 models vs the measured heat flow at the locations listed in table 3 and shown in fig. 18

Surface heat flow maps of the 4 models are shown in fig. 20 with heat flow measurements in the area, that were taken from the *Atlas of Geothermal Resources in Europe* (Hurter and Haenel, 2002) for comparison. The well locations in fig. 20 are numbered with the measured heat flow in mW/m^2. The wells in the north of the area show intermediate to high heat flow values. Further north, before the cyclades, a high value of 110 mW/m^2 was measured. In the central Aegean, on Samos and intermediate value of 60 mW/m^2 was measured. More to the south, in the cyclades and active volcanic arc, very high values are measured, reaching up to 625 mW/m^2 At the sea of Crete, the most southern part of the Area interest, another intermediate value of 70 mW/m^2 was measured. Outside of the area of interest, on crete, 2 lower intermediate values were measured as well.

Surface heat flow plots of the models at locations of certain relevant wells listed in table 3 are shown in fig. 21. The selection of the location was made to have at least one well per crust unit. In fig. 21 the top x-axis denotes heat flow. The red markers show the surface heat flow of each model and the green marker denotes the measured heat flow for comparison. Obviously, the highest heat flows are modeled by the scenarios with the shallowest LAB and the the lowest by the scenarios with the deepest LAB. Also, both figure 20 and 21, there is not necessarily 1 model that approximates the measured values well in every location.

In terms of surface heatflow, model 3 and 4 seem to fit the best to the northern part. The central and southern part with high to very high values show better fits with models 1 and 2, except for the measurement at Samos which is better represented by model 3 and 4.

4 Interpretation

Four 3-D lithospheric scale steady-state conductive thermal models, with different LAB depths, representing possible temperature distributions in the Aegean offshore region have been produced. Since there are no other differences in the models, the differences in temperature-depth and heat flow relations of the models can be attributed to the varying depth of their LAB's.

The shape of the heat generation profiles (Figure 19) can be explained by the succession of the lithologies that are present in the lithosphere at the locations of the wells, see fig. 12, 13 and 18. The abrupt decrease that all profiles show at a depth between 20-30 km correlates nicely with the depth of the Moho, where a lithotype of peridotite (see table 2) is assigned, which has a heat generation of 0.02 [$\mu W m^{-3}$]. At the locations of the wells where sediments are at the top of the lithosphere (12 and 41), an increase in radiogenic heat generation as well as thermal conductivity can be viewed. This is explained by the effect of compaction for the radiogenic heat generation and for the conductivity additionally the increase of temperature(through the temperature dependence of the conductivity). The profiles of location 11 and location 29, show similarities with the above mentioned locations. At location 11, this may have been caused an artefact of the resolution, since it is surrounded by sediments. But location 29 is in the Pelagonian region, see fig. 18, that isn't defined as a sedimentary basin, see table 2. However, it is explained by the fact that, although the Pelagonian unit was mentioned to be a crustal unit in section 2.2.2, it was assigned a sedimentary lithotype, see table 2. With these kind of lithotypes the radiogenic heat production and thermal conductivity are corrected for the effect of mechanical compaction and temperature with depth. The other locations, show profiles that are expected, with thermal conductivities that are slightly decreasing with depth due to an increase in temperature. Sometimes a small bump in the curve is shown, which is is caused by changes in lithologies. Looking at the shallow temperature maps, sharp changes are visible throughout the area. These can be correlated directly with the boundaries of the units and basins shown in for example fig. 18.

The coldest areas are in the regions where the Vardar- and Cycladic basement units surface. The initial conductivities of those units are within the same range, see table 2, but their radiogenic heat production differs significantly, with Vardar having the lowest radiogenic heat production of the two. Looking at the radiogenic heat production profiles of these regions in fig. 19, one can see that the heat production maintains a very low value to considerable depths (5-12 km) for wells 16, 24 and 26, located in the Vardar region. Whereas, at location 41, a constant radiogenic heat production is kept through almost the whole crust. Therefore, radiogenic heat production seems to be the biggest contributer to this difference. Not only for the top layers themselves, but also regarding the layers underneath them, see fig. 13. The lower crustal migmatite layer has a relatively high heat production and is present throughout a large part of the area, above the lithospheric mantle. The relatively high heat production, which is shown by the peaks in the radiogenic heat generation profiles shown in fig. 19 at depths before the radiogenic heat production drops to zero when crossing the Moho. One can see, in fig. 13 cross-section A, there is only a small portion of the migmatite layer present underneath the Vardar unit, but underneath the northern side of the Cycladic basement unit a thick portion of it is present, pinching out towards the south where the Cycladic basement unit lays directly on top of the Moho. In the shallow temperature maps of model 3 and 4, see fig. 17, it is visible the the Cycladic basement unit has a subtle fading temperature pattern towards the south.This is attributed to the pinching of the migmatite layer.

The Rhodope- and Pindos & CBU unit show intermediate temperatures. The Pindos & CBU unit is slightly warmer than the Rhodope Unit. In terms of thermal conductivity and radiogenic heat production, Rhodope has higher values for both. This seems to be compensated in the Pindos & CBU unit region by the relatively large amount of migmatite that is present underneath it, positioned at larger depths in the crust.

The hottest areas are viewed in the regions of the Pelagonian Unit and the Cretan basin. As mentioned earlier, the Pelagonian crustal unit was assigned a sedimentary lithotype in the input-model, not having a particularly high radiogenic heat production, as can be seen in table 2 and fig. 19 (the top of location 29). What both areas have in common regarding their thermal conductivity profiles is that at shallow depths their thermal conductivity decreases rapidly towards the top of the crust. This is thought be a bottleneck regarding the heat traveling to the top of the crust and being stalled at the shallow depths where the conductivity relatively becomes drastically lower, and is usually referred to as thermal blanketing. The behavior of the Pelagonian unit doesn't represent what would be expected from a crustal unit in terms of thermal conductivity, because it was assigned a sedimentary lithotype. Therefore, it should probably be improved to a more crustal-like lithotype, such as a metasediment.

The Thermaikos-, North Aegean Trough- and Northern Skyros Basins, which are located in the Vardar region, also show such a variation, but in this area the sediments in the basins already have a higher heat production than the underlying basement layer to begin with. This is different for the Cretan Basin where the underlying Cycladic basement unit has a higher heat production, but also has a higher thermal conductivity than the Cretan sediments before compaction.

At the location of the Ikaria Basin, a lower temperature is seen in the shallow temperature maps, this is explained by the high conductivity of the sediments before compaction, which is already higher than the Pelagonian unit which is underneath it, and therefore probably has an opposite effect on the heat traveling to the surface than in the case with the Cretan basin by transferring heat quicker to the top, rather than stalling it.

5 Discussion

Based on the existing literature, e.g. (Tirel et al., 2004; van Hinsbergen et al., 2005; Beniest et al., 2016; Brun et al., 2016; Menant et al., 2016), a 3-D model of the crust has been produced, see the map and cross-sections in fig. 12 and 13. The geometry of the crustal model is therefore only as good as the interpretations of the researches mentioned above and translation of them in this thesis to construct it, via the tools used and yet more interpretation. The northern part of the area was most cumbersome to constrain. For example, the Vardar unit could be placed elsewhere, or shaped differently, see fig. 4. This is also one off the coldest areas in the model. Some more research on this area is needed to better constrain its geometry and composition. There are some flaws that should be mentioned e.g. fig. 22. When using the GeoModeller software, the extrapolation, which is executed by the software, sometimes gave strange results. For example, sediments of the North Aegean Through Basin were put in places that weren't given as input. Depending to what depth of area they extent, those inaccuracies can have a significant effect on the results. It is expected that they can be overcome when structural input on the lithologies is imported with data-files instead of being drawn directly on the volume representing the area of interest. Unfortunately, these weren't available.

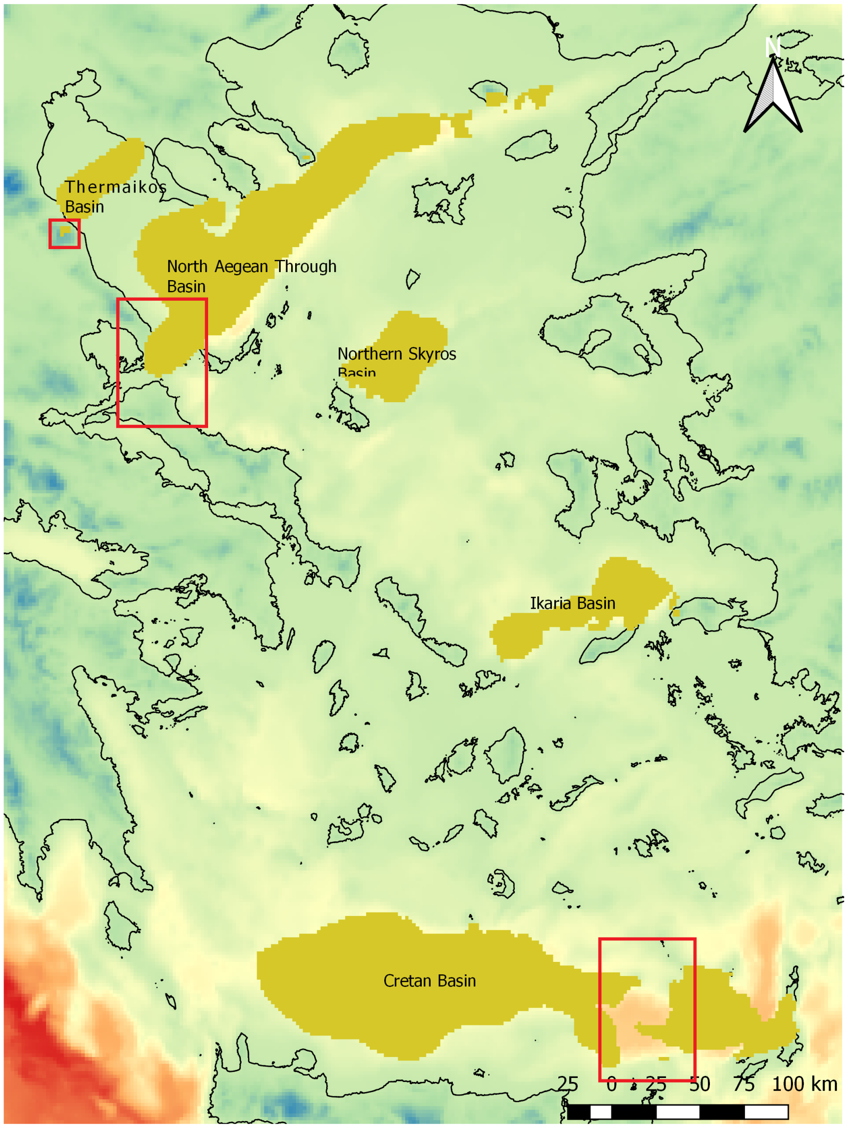

Figure 22: Example of difficulties constructing the geometrical model of the crust in GeoModeller. In the red rectangles, sediments have been left out or computed to far.

The choice of the composition of the crust, discussed in section 2.2, should only represent a first order approximation. For the scale of this research, it is not precisely constrained in the literature, but most certainly, the variability of the composition is way larger on a local scale than is emphasized in this thesis. It will therefore only affect the results very locally, which means that this wont play a significant role for the scale of this model. Nevertheless, going into such details was beyond the scope of this research.
Having constrained the crustal geometry and composition, an attempt has been done to model a first order approximation of the thermal structure of the area, only varying the depth of the LAB. The lower boundary condition of the models was the temperature at the LAB, that was set to 1330 °C for every model, (Limberger, 2018). The transition of lithosphere to asthenosphere is rather sharp boundary there is a large uncertainty in the temperature (1200-1330 °C) (Limberger, 2018). Therefore, it would be interesting to test other temperatures as well. Due to time limitations this has not been done in this research, and the choice was made to look at the most extreme case.

The upper boundary condition was a uniform surface temperature, that was set to 10 °C, since the largest part of the area is a shallow sea. A minor improvement that could applied is to construct a low resolution grid containing the surface temperatures of the area. The temperatures should be represented by averages, since one can not account for temporal hanges in these steady-state models. Starting with the islands, that are above sea-level and should probably have a higher surface temperatures and lower temperatures where deeper troughs are located. Although, this is not considered to have a large effect on the scale of this model it would still improve the results.

In terms of the resolution, the choice was made to use a horizontal cell-size of 5000 by 5000 [m] and a vertical cell-spacing of 400 [m], this is considered to be sufficient for a first order approximation and is reasonable regarding the computational time and power needed for the models. A higher resolution probably wouldn't improve the models significantly, with the small amount of layers and variability of lithotypes in the input-model, and would particularly take longer computationally.

Transient effects, such as, the time-dependent effect of recent extension, are unaccounted for, although it is certain that extension is going on at the moment and will probably have an effect on the thermal structure of the region. The heat flow measurements, from *The Atlas of Geothermal Resources in Europe* (Hurter and Haenel, 2002), were only used for a first order comparison with the modeled surface heat flows, but not for calibration of the models. This decision was made, because there is no data given on the depth of the wells, the conductivity and temperatures in the wells and the corrections on the measurements, therefore they were found to be not suitable for calibration.

Looking at the surface heat flow in the area, it should be noted that the population of well measurements that are shown in the area, see fig. 20, doesn't have a high density and may be only representative for small areas in the vicinity of them. But since this was the only data that were available in the timespan of this research, it is worthwhile to take them into account anyways. As mentioned in section 3, none of the models shows a perfect fit when comparing the outcomes with the measured heat flows. Although, in certain places, certain models fit better than others and vice versa. Very high heat flow measurements are shown in the area of the active volcanic arc, and are not represented by any of the models. Since the highest values are in area of the volcanic arc, this will probably be caused by convective heat transfer rather than conductive heat transfer, which would explain the large difference between the modeled surface heat flow and the measurements. Nevertheless, the area where the arc is located, is one of areas in the where the highest heat flow is modeled. However, the crust is also very thin in this region, which directly relates to a shallower LAB in that area in all of the models. This could explain the elevated heat flow in this area.

Jongsma (1974) already stated that the heat flow increases away from the Hellenic trench, which is outside of the modeled area, towards the north. This is also seen in the well measurements shown in fig. 20. From Crete where 2 well-measurements are shown, the heat flow increases towards the active volcanic arc. Qualitatively, this is also viewed in the models, but, as mentioned, they differ largely from the measurements in the volcanic arc.

Generally, if one were to say which of the 4 models from this research would represent heat flow of the Aegean sea, looking at the modeled surface heat flow maps and the measurements in fig. 20, models 3 and 4 show the best fit to the northern part of the area, model 2 for the central part and the southern part is represented best by model 1. Therefore, another improvement of on the lithosphere could be done by merging the lithospheric thicknesses of the corresponding models with the best fits, depending on the location. In the vicinity of the volcanic arc, local adjustment are suggested to model the heat flow in that area, such as constraining small areas and assigning them with a very high vertical conductivities to mimic the elevated heat flows that are measured in that area.

.

6 Conclusions

A geometrical model containing the main units and basins of the crust, that are of importance for geothermal modeling has been constructed, of which the northern part could be refined in a further mmodelling.

Based on the geometrical model, compositions and thermal properties were assigned to the units, inferred from the existing literature.

Four 3-D lithospheric scale steady-state conductive thermal models have been produced, with a fixed crust, only by varying the depth of the (thermal) LAB and therefore also the thickness of the lithospheric mantle.

None of the models represent the area entirely, in terms of surface heat flow. But in certain areas relative good fits have been shown with some of the models and it has been made clear that the Pelagonian unit should be represented by a lithotype that is more suitable for a crustal block in the input-model, than it is now.

In places, such as the Cyclades, other heat transfer mechanisms than conduction likely play a role and very locally may be the dominant mechanism.

Qualitatively, the models are in agreement with Jongsma (1974) about the heat flow pattern from the south towards the Cycladic volcanic arc.

Acknowledgements

I would like to thank the following people for contributing to my thesis research and supporting me during the process. It has meant a great deal to me.

- dr. Damien Bonté
- dr. Fred Beekman
- dr. J. Limberger
- prof. dr. D. Sokoutis
- dr. C. Tirel
- prof. dr. J. P. Brun
- Loes Vaessen
- Eszter Békési
- Yola Hesselberth
- Kat Sejan
- dr. J.W.H. Smit
- dr. A. Beniest
- Ahmad Purwandono
- Lukman Sutrisno
- Kristóf Porkoláb

References

Amante, C. and Eakins, B. (2009). ETOPO1 1 Arc-Minute Global Relief Model: Procedures, Data Sources and Analysis. *NOAA Technical Memorandum NESDIS NGDC-24*, (March):19.

Beniest, A., Brun, J. P., Gorini, C., Crombez, V., Deschamps, R., Hamon, Y., and Smit, J. (2016). Interaction between trench retreat and Anatolian escape as recorded by neogene basins in the northern Aegean Sea. *Marine and Petroleum Geology*, 77:30–42.

Bonneau, M. and Kienast, J. R. (1982). Subduction, collision et schistes bleus: l'exemple de l'Egée (Grèce). *Bulletin de la Société Géologique de France*, 24(4):785–791.

Brun, J. P. and Faccenna, C. (2008). Exhumation of high-pressure rocks driven by slab rollback. *Earth and Planetary Science Letters*, 272(1-2):1–7.

Brun, J. P., Faccenna, C., Gueydan, F., Sokoutis, D., Philippon, M., Kydonakis, K., Gorini, C., and Polat, A. (2016). The two-stage Aegean extension, from localized to distributed, a result of slab rollback acceleration. *Canadian Journal of Earth Sciences*, 53(11):1142–1157.

Brun, J. P. and Sokoutis, D. (2007). Kinematics of the Southern Rhodope Core Complex (North Greece). *International Journal of Earth Sciences*, 96(6):1079–1099.

Brun, J. P. and Sokoutis, D. (2010). 45 m.y. of Aegean crust and mantle flow driven by trench retreat. *Geology*, 38(9):815–818.

Chapman, D. S. (1986). Thermal gradients in the continental crust. *Geological Society, London, Special Publications*, 24(1):63–70.

Earle, S. (2015). *Physical Geology*.

Faccenna, C., Jolivet, L., Piromallo, C., and Morelli, A. (2003). Subduction and the depth of convection in the Mediterranean mantle. *Journal of Geophysical Research: Solid Earth*, 108(B2).

Fytikas, M., Innocenti, F., Manetti, P., Peccerillo, a., Mazzuoli, R., and Villari, L. (1984). Tertiary to Quaternary evolution of volcanism in the Aegean region. *Geological Society, London, Special Publications*, 17(1):687–699.

Gautier, P., Brun, J. P., Moriceau, R., Sokoutis, D., Martinod, J., and Jolivet, L. (1999). Timing, kinematics and cause of Aegean extension: A scenario based on a comparison with simple analogue experiments. *Tectonophysics*, 315(1-4):31–72.

Hantschel, T. and Kauerauf, A. I. (2009). *Fundamentals of basin and petroleum systems modeling*. Springer Berlin Heidelberg, Berlin, Heidelberg.

Hsü, K. J., Montadert, L., Bernoulli, D., Bizon, G., Cita, M. B., Erickson, A., Fabricius, F., Garrison, R. E., Kidd, R. B., Melieres, F., Muller, C., and Wright, R. C. (1978). 8. Site 378: Cretan Basin. *Deep Sea Drillings Initial Reports*, 42:321–357.

Hurter, S. and Haenel, R., editors (2002). *Atlas of Geothermal Resources in Europe.*

Jolivet, L. and Brun, J. P. (2010). Cenozoic geodynamic evolution of the Aegean. *International Journal of Earth Sciences*, 99(1):109–138.

Jolivet, L. and Faccenna, C. (2000). Mediterranean extension and the Africa-Eurasia collision. *Tectonics*, 19(6):1095–1106.

Jolivet, L., Faccenna, C., Huet, B., Labrousse, L., Le Pourhiet, L., Lacombe, O., Lecomte, E., Burov, E., Denèle, Y., Brun, J. P., Philippon, M., Paul, A., Salaün, G., Karabulut, H., Piromallo, C., Monié, P., Gueydan, F., Okay, A. I., Oberhänsli, R., Pourteau, A., Augier, R., Gadenne, L., and Driussi, O. (2013). Aegean tectonics: Strain localisation, slab tearing and trench retreat. *Tectonophysics*, 597-598:1–33.

Jolivet, L., Famin, V., Mehl, C., Parra, T., Aubourg, C., Hébert, R., and Philippot, P. (2004). Progressive strain localisation, boudinage and extensional metamorphic complexes, the Aegean Sea Case, in Whitney D.L., Teyssier C. and Siddoway C.S., Gneiss domes in orogeny : Boulder, Colorado. *Geological Society of America Special Papers*, pages 185–210.

Jongsma, D. (1974). Heat Flow in the Aegean Sea. *Geophysical Journal International*, 37(3):337–346.

Kruckenberg, S. C., Vanderhaeghe, O., Ferré, E. C., Teyssier, C., and Whitney, D. L. (2011). Flow of partially molten crust and the internal dynamics of a migmatite dome, Naxos, Greece. *Tectonics*, 30(3):1–24.

Le Pichon, X. and Angelier, J. (1979). The hellenic arc and trench system: A key to the neotectonic evolution of the eastern mediterranean area. *Tectonophysics*, 60(1-2):1–42.

Le Pichon, X., Angelier, J.-P., Osmaston, M. F., and Stegena, L. (1981). The Aegean Sea. *Philosophica Transactions of the Royal Society of London. Series A, Mathematical and Physical Sciences,*, 300(1454):357–372.

Limberger, J. (2018). *Thermo-mechanical characterisation of the lithosphere: Implications for geothermal resources.* PhD thesis, Utrecht University, Utrecht.

Limberger, J., van Wees, J. D., Tesauro, M., and Smit, J. (2018). Unravelling the thermo-mechanical structure of the European lithosphere by inversion of subsurface temperature data.

Makris, J., Papoulia, J., and Yegorova, T. (2013). A 3-D density model of greece constrained by gravity and seismic data. *Geophysical Journal International*, 194(1):1–17.

McClusky, S., Balassanian, S., Barka, A., Demir, C., Ergintav, S., Georgiev, I., Gurkan, O., Hamburger, M., Hurst, K., Kahle, H., Kastens, K., Kekelidze, G., King, R., Kotzev, V., Lenk, O., Mahmoud, S., Mishin, A., Nadariya, M., Ouzounis, A., Paradissis, D., Peter, Y., Prilepin, M., Reilinger, R., Sanli, I., Seeger, H., Tealeb, A., Toksöz, M. N., and Veis, G. (2000). Global Positioning System constraints on plate kinematics and dynamics in the eastern Mediterranean and Caucasus. *Journal of Geophysical Research*, 105(B3):5695.

McKenzie, D. (1978). Some remarks on the development of sedimentary basins. *Earth and Planetary Science Letters*, 40(1):25–32.

Menant, A., Jolivet, L., and Vrielynck, B. (2016). Kinematic reconstructions and magmatic evolution illuminating crustal and mantle dynamics of the eastern Mediterranean region since the late Cretaceous. *Tectonophysics*, 675:103–140.

Mitropoulos, P. and Tarney, J. (1992). Significance of mineral composition variations in the Aegean Island Arc. *Journal of Volcanology and Geothermal Research*, 51(4):283–303.

Philippon, M., Brun, J. P., and Gueydan, F. (2012). Deciphering subduction from exhumation in the segmented Cycladic Blueschist Unit (Central Aegean, Greece). *Tectonophysics*, 524-525:116–134.

Philippon, M., Brun, J. P., Gueydan, F., and Sokoutis, D. (2014). The interaction between Aegean back-arc extension and Anatolia escape since Middle Miocene. *Tectonophysics*, 631(C):176–188.

Schatz, J. F. and Simmons, G. (1972). Thermal conductivity of Earth materials at high temperatures. *Journal of Geophysical Research*, 77(35):6966–6983.

Sekiguchi, K. (1984). A method for determining terrestrial heat flow in oil basinal areas. *Tectonophysics*, 103(1-4):67–79.

Tirel, C., Gueydan, F., Tiberi, C., and Brun, J. P. (2004). Aegean crustal thickness inferred from gravity inversion. Geodynamical implications. *Earth and Planetary Science Letters*, 228(3-4):267–280.

van Hinsbergen, D. J. J., Hafkenscheid, E., Spakman, W., Meulenkamp, J. E., and Wortel, R. (2005). Nappe stacking resulting from subduction of oceanic and continental lithosphere below Greece. *Geology*, 33(4):325–328.

Xu, Y., Shankland, T. J., Linhardt, S., Rubie, D. C., Langenhorst, F., and Klasinski, K. (2004). Thermal diffusivity and conductivity of olivine, wadsleyite and ringwoodite to 20 GPa and 1373 K. *Physics of the Earth and Planetary Interiors*, 143(1-2):321–336.